

Evolution of the Inner Accretion Flow in Swift J1727.8–1613 across Intermediate States: Insights from Broadband Spectral and Timing Analysis

SWADESH CHAND,^{1,2} ANDRZEJ A. ZDZIARSKI,³ GULAB C. DEWANGAN,¹ AND PRAGATI SAHU⁴

¹*Inter-University Centre for Astronomy and Astrophysics, Pune, Maharashtra-411007, India*

²*Institute of Astronomy, National Tsing Hua University, Hsinchu 300044, Taiwan*

³*Nicolaus Copernicus Astronomical Center, Polish Academy of Sciences, Bartycka 18, PL-00-716 Warszawa, Poland*

⁴*Department of Pure and Applied Physics, Guru Ghasidas Vishwavidyalaya (A Central University), Bilaspur (C. G.)—495009, India*

ABSTRACT

We present a comprehensive broadband spectral and variability study of the newly detected black hole X-ray binary Swift J1727.8–1613 in the intermediate states during its 2023 outburst, using multi-mission observations from NICER, NuSTAR, AstroSat, and Insight-HXMT. The spectral data up to 78 keV in the hard-intermediate state (HIMS) requires models with two Comptonizing regions. In contrast, models with a single Comptonizing region adequately describe the soft-intermediate states (SIMS), implying a significant evolution in the disk-corona geometry between the states. The hard X-ray tail above 100 keV in the HIMS, detected with both AstroSat/CZTI and Insight-HXMT/HE, indicates that the electron population in the corona is not purely thermal but rather hybrid, with a power-law distribution above the thermal cutoff. While both the reflection modeling and disk continuum fitting favor a truncated disk geometry in the HIMS, the disk substantially moves close to the innermost stable circular orbit in the SIMS, accompanied by a significant rise in the disk temperature. This interpretation is further supported by the increase in the QPO frequency from ~ 1.3 to ~ 6.6 Hz. From joint modeling of the disk continuum and reflection component, we estimate a black hole mass of $10.5^{+7.7}_{-3.0}$, spin of $0.79^{+0.03}_{-0.13}$, and disk inclination angle of 42° – 50° , which match well with the previously reported spectro-polarimetric measurements. The inferred source distance of ~ 3.5 kpc is consistent with the recent estimate based on optical spectroscopy. We find a weakly variable or stable disk and a highly variable Comptonized component.

Keywords: High energy astrophysics — Low-mass X-ray binary — Stellar mass black holes — X-ray sources

1. INTRODUCTION

Transient low-mass black hole X-ray binaries (BHXRBs) exhibit substantial evolution in their accretion geometry, particularly in the corona and accretion disk’s size and shape, across different spectral states during sporadic outbursts. These spectral state transitions are typically traced using the hardness–intensity diagram (HID), which follows a characteristic q-shaped track based on the changes in the source hardness with count rates in an anti-clockwise manner (Homan et al. 2001; Belloni et al. 2005; Homan & Belloni 2005; Fender

et al. 2009; Belloni 2010; Belloni et al. 2011). During a typical outburst, BHXRBs spend most of their time in either the low/hard state (LHS) or the high/soft state (HSS), with relatively brief excursions through the short-lived HIMS and the SIMS.

The accretion geometry in the HSS is now well understood, with a standard optically thick and geometrically thin accretion disk (Shakura & Sunyaev 1973) extending close to the innermost circular orbit (ISCO). This state is characterized by thermal disk emission peaking at ≈ 1 keV and low levels of X-ray variability. In contrast, the LHS is dominated by Comptonized hard X-ray emission from a hot corona and exhibits strong variability. However, the geometry of the inner accretion flow in the LHS remains debated, particularly regarding whether the disk extends to the ISCO or is truncated at

a large radius by a radiatively inefficient inner hot flow (Miller et al. 2006, 2008; Done & Gierliński 2006; Reis et al. 2008; Done & Diaz Trigo 2010; Kolehmainen et al. 2014; Bambi et al. 2021, for a review).

The HIMS and SIMS are transitional phases, where significant contributions from both the disk and coronal emission are found in the observed spectrum. The HIMS typically shows relatively strong Comptonized emission and large variability, with often detection of type-C quasi-periodic oscillations (QPOs; Casella et al. 2004, 2005). As the mass accretion rate increases, a source starts transitioning towards the SIMS, and the disk moves close to the ISCO (Done et al. 2007; Belloni et al. 2011). The observed spectrum is then dominated by the thermal emission from the disk, and the source variability becomes weaker in comparison to the HIMS. Type-B QPOs, which are relatively broader than the Type-C ones, are sometimes detected in the SIMS. Hence, the study of these intermediate states offers crucial insights into the dynamics of the inner accretion flow. However, BHXRBS do not always evolve through all four canonical spectral states during an outburst. In some cases, the source remains in the LHS throughout the entire outburst, likely due to a rapid change or insufficient rise in the mass accretion rate. Such events are referred to as hard-only or failed outbursts (Capitanio et al. 2009; Stiele & Yu 2016; Sahu et al. 2024).

The hard X-ray emission observed in BHXRBS is commonly attributed to thermal Comptonization, which originates from the inverse Compton scattering of soft disk photons by hot electrons in the corona. The electron distribution is predominantly thermal or Maxwellian at a mildly relativistic temperature and shows a sharp cutoff at ≈ 100 keV, particularly in the LHS (Done et al. 2007; Zdziarski et al. 2020). However, growing observational evidence for the presence of hard X-ray tails extending well beyond the thermal cutoff in several BHXRBS in the intermediate and soft spectral states suggests that the coronal electron population also includes a significant fraction of non-thermal electrons, with a power-law distribution (McConnell et al. 2000, 2002; Wardziński et al. 2002; Cadolle Bel et al. 2006; Poutanen & Vurm 2009; Jourdain et al. 2012; Cangemi et al. 2021, 2023). Similar non-thermal hard X-ray tail has also been reported in the LHS of the bright low-mass BHXRBS MAXI J1820+070 (Zdziarski et al. 2021c). Such a hybrid electron distribution, comprising thermal and non-thermal electron populations, can significantly modify the shape of the Comptonized spectrum (Poutanen & Vurm 2009; Gierliński et al. 1999; Zdziarski et al. 2001). While the Comptonization due to thermally distributed electrons dominates the low-

energy part of the spectrum, the high-energy excess beyond the thermal cutoff can be described by the Comptonization associated with the non-thermal electron distribution. Moreover, the non-thermal electron population can enhance electron-positron pair production, thereby introducing a thermostat effect that regulates and potentially lowers the coronal electron temperature (Zdziarski et al. 2021c).

Another important component of the X-ray spectra of BHXRBS is the reflection emission, which arises due to the reflection of hard coronal X-rays by the disk. The reflection spectrum comprises mainly the iron K_α emission line, peaking at 6–7 keV, photoelectric absorption at low energies, and the reflection hump at 20–30 keV originating due to Compton scattering of the high-energy photons. Gravitational redshift and the Doppler effect can distort the shape of the iron K_α line if the reflecting material is close to the ISCO (Fabian et al. 1989). The modeling of this reflection spectrum is one of the main approaches to estimate the spin of the black hole, independent of the black hole mass and source distance. Another widely used method for estimating black hole spin is the disk continuum modeling, which requires prior knowledge of the black hole mass and source distance. Both of these methods rely on the assumption that the accretion disk is at the ISCO or at least very close to it, which is usually observed in the soft state. Furthermore, the presence of a high-energy tail in the soft state, which produces the relativistic reflection features, allows us to constrain the black hole spin by modeling the reflection component and disk continuum together (Chand et al. 2022; Zdziarski et al. 2024a,b). A detailed overview of the different methods of spin estimation is provided in a recent review paper by Zdziarski et al. (2025a).

The bright low-mass X-ray transient Swift J1727.8–1613 was first detected on 2023 August 24 (Kennea & Swift Team 2023; Negoro et al. 2023; Page et al. 2023), with the source flux reaching a peak of ~ 7 Crab in the 15–50 keV band (Palmer & Parsotan 2023). Optical follow-up observations identified the source as a low-mass BHXRBS residing at a distance of 3.4 ± 0.3 kpc, with an orbital period of about ~ 10 hours (Mata Sánchez et al. 2025). Based on reflection modeling in the LHS, Peng et al. (2024) reported a nearly maximally spinning black hole having a mass of $\sim 10M_\odot$ and a disk inclination of $\sim 40^\circ$. Later, Svoboda et al. (2024) estimated the black hole spin to be 0.87 ± 0.03 by jointly modeling the disk continuum and reflection component in the HSS. From polarimetric measurements, the authors suggested an inclination angle in the range of $30^\circ - 50^\circ$. Using a new analytical model to fit the spatial structure of the jet, Zdziarski et al. (2025b) also favored a black

hole mass below $13 M_{\odot}$ and a distance less than 5 kpc for this source. Additionally, a substantial variation in the polarization degree across different spectral states, implying an evolution in the inner accretion flow, is also observed in this source (Veledina et al. 2023; Svoboda et al. 2024). The polarization studies also suggest that the corona is radially extended in the disk plane and lies perpendicular to the jet axis (Veledina et al. 2023; Ingram et al. 2024). Apart from this, Liu et al. (2024) showed that the broadband spectrum of Swift J1727.8–1613 in the LHS is complex and requires Comptonization from a hybrid electron distribution. While the authors found the contribution from non-thermal electrons to be small in the LHS, it increased as the source moved toward the spectral transition. The QPO frequencies were also found to be evolving from ~ 1.4 to ~ 2.6 Hz over the HIMS (Nandi et al. 2024) and ~ 0.2 Hz to ~ 1.86 Hz over the transitioning period from the intermediate to the soft states (Chatterjee et al. 2024). Similar evolution in the QPO frequencies from ~ 0.3 Hz in the LHS to ~ 7 Hz in the HIMS, along with a shrinkage in the coronal shape and disk truncation radius from $30\text{--}40 r_g$ to $10 r_g$, was also reported using NICER observations (Rawat et al. 2025).

In this work, we carry out a detailed broadband spectral and timing study of the newly discovered low-mass BHXRB Swift J1727.8–1613 using multi-mission observations from NICER, NuSTAR, AstroSat, and Insight-HXMT during two distinct spectral states: the HIMS and SIMS. We demonstrate that the spectral data up to 78 keV in the HIMS requires models with two physically distinct thermal Comptonizing regions. Unlike previous studies in the LHS, our analysis of the extended broadband spectrum up to 200 keV reveals that the hard X-ray tail in the HIMS becomes prominent only above ~ 100 keV. This spectral behavior cannot be accounted for by thermal Comptonization alone and instead requires a hybrid Comptonization model involving both thermal and non-thermal electron populations, underscoring the complex nature of the corona. We also show that the disk-corona geometry evolves significantly across the two observations. Utilizing broadband X-ray data in the SIMS, we estimate key parameters such as mass and spin of the black hole, disk inclination, and source distance using different models for the accretion disk, and examine the model dependence of these parameters. In addition, we investigate the variability properties of the source in both the HIMS and SIMS through a detailed analysis of the power density spectra (PDS) and rms–energy spectra. The paper is organized as follows. Section 2 describes the observations and data reduction. In Section 3, we present the results from our

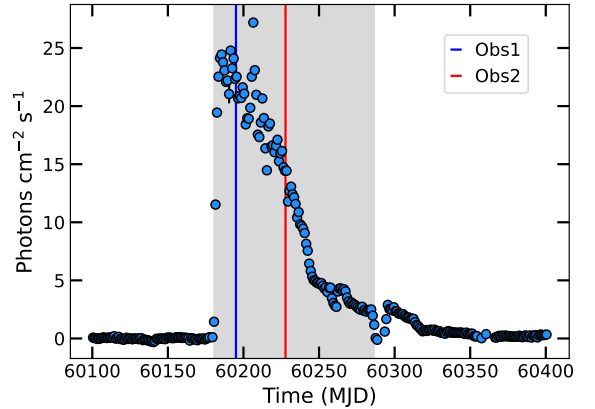


Figure 1. MAXI long-term lightcurve in the 2 – 20 keV band during the outburst of Swift J1727.8–1613 in 2023. The vertical lines indicate the positions of the two sets of observations considered in this work. The shaded region is the period that has been used to derive the HID in Figure 2.

spectral and timing analysis. We discuss the implications of our findings in Section 4, and summarize our conclusions in Section 5.

2. OBSERVATIONS AND DATA REDUCTION

We analyze two distinct sets of observations of the recently discovered low-mass BHXRB SWIFT J1727.8–1613, obtained during its 2023 outburst using NICER, NuSTAR, AstroSat, and Insight-HXMT. These data sets were likely taken during the intermediate states (see below) and remain unexplored in terms of broadband spectral modeling and detailed variability studies. The first dataset comprises simultaneous observations with NICER and NuSTAR, and is complemented by data from AstroSat and Insight-HXMT, providing broadband spectral coverage up to 200 keV near the peak of the outburst. The second dataset includes contemporaneous observations with NICER and NuSTAR, acquired during the decay phase of the outburst. Details of these observations are summarized in Table 1, and their positions within the outburst are indicated on the long-term MAXI light curve of the source, as shown in Figure 1.

To obtain an initial insight into the spectral states of the source during the two observations, we derived HID using the MAXI observations of Swift J1727.8–1613 over the shaded interval in Figure 1, covering the entire 2023 outburst. We first calculated the hardness ratio (HR) by dividing the count rate in the 4–10 keV band by that in the 2–4 keV band. The HID was then obtained by plotting the HR against the MAXI count rate in the 2–20 keV band. Figure 2 displays the resulting HID, which indicates that the source underwent a full spectral transition during this outburst. The approximate positions

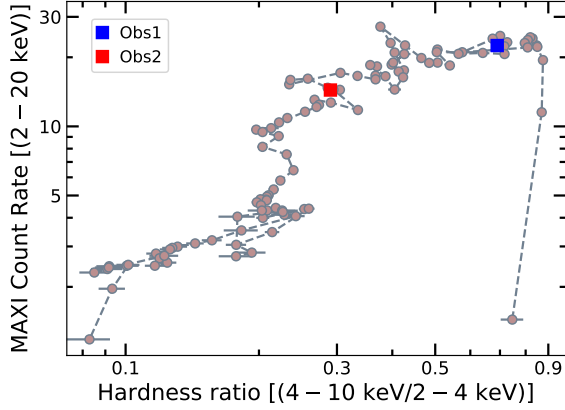


Figure 2. HID derived using MAXI observations (shaded region of Figure 1) of the 2023 outburst of Swift J1727.8–1613. The squares mark the positions of the NICER observations used in this work, overplotted on the HID.

of the two NICER observations analyzed in this study are overplotted on the HID based on their respective start times. These positions suggest that the source was likely in the HIMS during Obs1, characterized by an HR of ~ 0.7 , and possibly transitioned to the SIMS during Obs2, with the HR decreasing to ~ 0.3 .

2.1. NICER

We processed the NICER (Gendreau et al. 2016) observations using the standard task `nicer12` available within HeaSoft (v.6.34) and the most recent CALDB (v.xti_20240206). To extract the time-averaged source and background energy spectra, we used the standard script `nicer13-spec`, where the background spectra are estimated using the ‘3C50’ model. We further used the `nicer13-lc` task to generate the lightcurves from both the observations.

2.2. NuSTAR

The NuSTAR (Harrison et al. 2013) data were processed using the standard task `nupipeline`, which is part of the NuSTARDAS software package, along with the latest calibration files. Since the source was very bright during these observations, we applied the status expression `statusexpr='(STATUS==b0000xxx00xxxx000)&&(SHIELD==0)'` during data processing. Source and background spectra were then extracted considering circular regions of $70''$ radius, centered at the source position and an off-source region, respectively, using the standard task `nuproducts`. The corresponding response matrix files (RMFs) and auxiliary response files (ARFs) were generated using the same task. It is worth noting that the NuSTAR detectors may be affected by dead

time¹, particularly for bright sources. While dead time does not have any effect on spectroscopy, it can significantly impact timing studies (Bachetti et al. 2015; Bachetti & Huppenkothen 2018, for details on NuSTAR dead time).

2.3. AstroSat/CZTI

AstroSat, India’s first multi-wavelength astronomy satellite, was launched on September 28, 2015. It carries four co-aligned instruments onboard: the Soft X-ray Telescope (SXT; Singh et al. 2016, 2017), the Large Area X-ray Proportional Counter Array (LAXPC; Yadav et al. 2016a,b; Agrawal et al. 2017; Antia et al. 2017), Cadmium-Zinc-Telluride Imager (CZTI) (Vadawale et al. 2016; Vibhute et al. 2021), and the Ultra-Violet Imaging Telescope (UVIT; Tandon et al. 2017, 2020). For this study, we utilized data exclusively from the CZTI instrument. We downloaded the CZTI data from the AstroSat data archive² and produced clean event files using the latest version of the `cztpipeline` (v3.0)³ and updated calibrations. This version of the `cztpipeline` includes an improved mask-weighting technique implemented in the `cztbindata` module (Chattopadhyay et al. 2024). The clean event files were then used to extract background-subtracted spectra for each quadrant using the standard tasks within `cztpipeline`⁴. Finally, spectra from all four quadrants were combined to produce a high signal-to-noise ratio spectrum. We then added a 2% systematic error to the CZTI merged spectral data to account for the calibration uncertainties of the instrument. We analyzed the CZTI spectral data in the 40–200 keV band, excluding data below 40 keV due to the strong presence of Xe hump, which peaks around ~ 30 keV.

2.4. Insight-HXMT/HE

The first X-ray satellite of China, Insight-HXMT (Zhang et al. 2014, 2018, 2020), launched on June 15, 2017, carries three different payloads onboard, and they are: Low-Energy X-ray Telescope (LE; Chen et al. 2020), Medium-Energy X-ray Telescope (ME; Cao et al. 2020), and High-Energy X-ray Telescope (HE; Liu et al. 2020). Here, we have utilized the data only from HE, which operates in the 20 – 250 keV band, for spectral analysis. We used HXMTDAS (v.2.06; Zhao 2020) pack-

¹ It is the interval after each detected event during which the instrument processes the signal and cannot record new photons.

² https://astrobrowse.issdc.gov.in/astro_archive/archive/Home.jsp

³ <http://astrosat-ssc.iucaa.in/cztiData>

⁴ http://astrosat-ssc.iucaa.in/uploads/threadsPageNew_SXT.html

Table 1. List of Observations of SWIFT J1727.8–1613

Obs No	Instrument	Obs ID	Start Time (yyyy-mm-dd)	Stop Time (yyyy-mm-dd)	Eff. Exp.(s)
Obs1	NICER	6750010502	2023-09-08 00:47:12	2023-09-08 13:13:35	2270
	NuSTAR/FPMA	80902333008	2023-09-08 00:56:09	2023-09-08 04:01:09	543.2
	FPMB	...	2023-09-08 00:56:09	2023-09-08 04:01:09	589.5
	AstroSat/CZTI	9000005836	2023-09-08 01:39:59	2023-09-09 00:23:28	26770
	Insight-HXMT/HE	P061433800901	2023-09-08 02:13:25	2023-09-08 05:37:26	2235
Obs2	NICER	6203980136	2023-10-09 03:45:39	2023-10-09 16:16:20	1909
	NuSTAR/FPMA	80902313016	2023-10-10 19:36:09	2023-10-10 23:06:09	1065
	FPMB	...	2023-10-10 19:36:09	2023-10-10 23:06:09	1138

age to process the HE data following the standard procedure and default inputs. For the generation of source and background spectra and the response files, the standard task `hpipeline` has been used. For this study, we utilized the HE spectral data in the 30–150 keV band and discarded the data below 30 keV due to calibration issues, and beyond 150 keV for significant background contamination.

3. ANALYSIS AND RESULTS

3.1. Broadband Spectral Analysis

We performed broadband spectral analysis using XSPEC (v.12.14.1; [Arnaud 1996](#)) and quoted all the uncertainties on the best-fit parameters at the 90% confidence ($\Delta\chi^2 \approx 2.71$) level. We used the optimal binning algorithm ([Kaastra & Bleeker 2016](#)) with a minimum of 25 counts per grouped bin to the NICER, NuSTAR, and HE spectral data to enable the use of χ^2 statistics. For the CZTI spectral data, we retained the default binning criteria embedded in the `cztpipeline` ([Chattopadhyay et al. 2024](#); [Chand et al. 2024](#)). To account for any differences in the relative normalizations and possible calibration uncertainties between the different instruments, we multiplied a `plabs` component to our models. This component is purely phenomenological and does not alter the intrinsic shape of the continuum or the key physical parameters. The parameters $\Delta\Gamma$ and K of the `plabs` component were fixed at 0 and 1, respectively, for NuSTAR FPMA, while they were varied freely for the other instruments. We started the spectral analysis by jointly fitting the simultaneous (for Obs1) or contemporaneous (for Obs2) NICER and NuSTAR spectral data in the 0.7 – 78 keV band with a model consisting of a multicolor disk blackbody component (`diskbb`; [Mitsuda et al. 1984](#)) to account for the thermal emission from the disk, and `thcomp` ([Zdziarski et al. 2020](#)), describing the spectra from Comptonization of the disk photons by thermal electrons in the corona. As `thcomp` is a convolution model, we extended

the sample energy range from 0.01 to 1000 keV using the `energies` command within XSPEC. Furthermore, we treated the absorption by the interstellar medium using the Galactic absorption component `tbabs` with the abundances and cross sections taken from [Wilms et al. \(2000\)](#) and [Verner et al. \(1996\)](#), respectively. This model `plabs*tbabs(thcomp*diskbb)` provided a very poor spectral fit and left prominent residuals at the Fe K_α band and reflection hump region, typically arising due to the reflection of the coronal irradiation from the accretion disk. Figure 3 shows the NuSTAR/FPMA spectral data for the two different spectral states along with the data residuals to the model `tbabs(thcomp*diskbb)`. A clear difference in the spectral nature between the two spectral states can be seen from this figure. The nature of the reflection hump also shows a transition over the two observations, where it appears to be relatively prominent at high energies in the Obs1 and weak in the Obs2.

3.1.1. HIMS

For Obs1, we then attempted to model reflection from ionized material by convolving `ireflect` with `thcomp` and incorporating a `gaussian` component to account for the Fe K_α emission line. The `ireflect` model is the generalized convolution form of `pexriv`, and describes only the hard X-ray shape of the reflected spectrum, excluding all the line emissions. However, this model configuration, `plabs*tbabs(ireflect*thcomp*diskbb+gaussian)`, yielded a statistically poor fit, with $\chi^2/dof = 1634.4/596$, and left significant residuals at high energies. This indicates that a model involving a single Comptonizing region is insufficient to reproduce the observed broadband spectral shape, and an additional Comptonization component may be required to account for the high-energy excess. A requirement for two distinct Comptonizing regions to describe the broadband (0.7 – 100 keV) spectrum in the LHS of the

Table 2. Best-fit broadband X-ray spectral parameters derived for Obs1 (HIMS)

Component	Parameter	M1	M2	M3
		NICER/NuSTAR	NICER/NuSTAR	NICER/NuSTAR/HE/CZTI
TBabs	$N_{\text{H}} (10^{22} \text{ cm}^{-2})$	0.30 ± 0.02	0.27 ± 0.01	0.27 ± 0.01
Diskbb	$kT_{\text{in}} \text{ (keV)}$	0.39 ± 0.02	0.40 ± 0.01	0.39 ± 0.01
	norm ($\times 10^5$)	$1.96^{+0.25}_{-0.75}$	$1.54^{+0.49}_{-0.40}$	$1.61^{+0.27}_{-0.29}$
Thcomp	Γ	$1.95^{+0.03}_{-0.09}$	$1.92^{+0.04}_{-0.17}$	1.90 ± 0.04
	$kT_{\text{e}} \text{ (keV)}$	$4.43^{+0.19}_{-0.21}$	$4.6^{+0.26}_{-0.25}$	4.77 ± 0.18
	C_{f}	$0.45^{+0.03}_{-0.05}$	$0.43^{+0.10}_{-0.13}$	0.40 ± 0.04
RelxillCp	Γ	$1.80^{+0.05}_{-0.16}$
	$kT_{\text{e}} \text{ (keV)}$	$15.95^{+1.68}_{-0.93}$
	$R_{\text{in}} (r_{\text{g}})$	$143.7_{-110.4}$
	$\log \xi$	$3.69^{+0.12}_{-0.11}$
	$A_{\text{Fe}} \text{ (solar)}$	$0.61^{+0.44}$
	$\log N$	$15.98^{+0.51}$
	R_{ref}	$0.64^{+0.44}_{-0.20}$
	norm	$0.17^{+0.05}_{-0.03}$
mbknp	B	$1.0^{+0.12}$
	I	0.3^f
Relconv	$R_{\text{in}} (r_{\text{g}})$...	$249.5_{-196.4}$	$212.6_{-168.8}$
Xilconv	R_{ref}	...	$0.17^{+0.02}_{-0.03}$	$0.15^{+0.04}_{-0.03}$
	$A_{\text{Fe}} \text{ (solar)}$...	1^f	1^f
	$\log \xi$...	$3.89^{+0.11}_{-0.09}$	3.84 ± 0.08
Compps [thermal/hybrid]	$kT_{\text{e}} \text{ (keV)}$...	$15.32^{+0.84}_{-0.58}$	$13.73^{+0.32}_{-0.43}$
	τ	...	$9.7_{-2.2}$	$9.96^{+1.19}_{-0.83}$
	γ_{min}	1.33 ± 0.01
	norm ($\times 10^4$)	...	$5.7^{+2.3}_{-2.4}$	$7.5^{+0.9}_{-1.5}$
Flux _{0.001–500 keV} ^{unabs} [$10^{-7} \text{ erg cm}^{-2} \text{ s}^{-1}$]		~ 3.3	~ 3.3	~ 3.4
Cross-calibration	$\Delta\Gamma_{\text{NICER}}$	0.08 ± 0.01	0.08 ± 0.01	0.08 ± 0.01
	K_{NICER}	0.86 ± 0.02	0.86 ± 0.02	0.86 ± 0.02
	$\Delta\Gamma_{\text{NuSTAR B}}$	$0.004^{+0.005}$	$0.004^{+0.005}$	$0.004^{+0.005}$
	$K_{\text{NuSTAR B}}$	0.97 ± 0.01	0.97 ± 0.01	0.97 ± 0.01
	$\Delta\Gamma_{\text{HE}}$	< 0.03
	K_{HE}	$0.94^{+0.01}_{-0.10}$
	$\Delta\Gamma_{\text{CZTI}}$	$0.10^{+0.02}_{-0.04}$
	K_{CZTI}	$0.63^{+0.06}_{-0.08}$
χ^2/dof		457.3/589	458.7/592	601.5/681

Notes – M1: `plabs*tbabs(thcomp*diskbb+mbknp*relxillCp)`, M2: `plabs*tbabs*relconv*xilconv(thcomp*diskbb+compps[thermal])`, M3: `plabs*tbabs*relconv*xilconv*(thcomp*diskbb+compps[hybrid])`, where the spectral data from HE and CZTI were also added. See Svoboda et al. (2024) for the definition of the `mbknp` in `xspect`. The spin of the black hole and disk inclination angle are fixed at 0.998 and 40° , respectively. ^f – indicates fixed parameters.

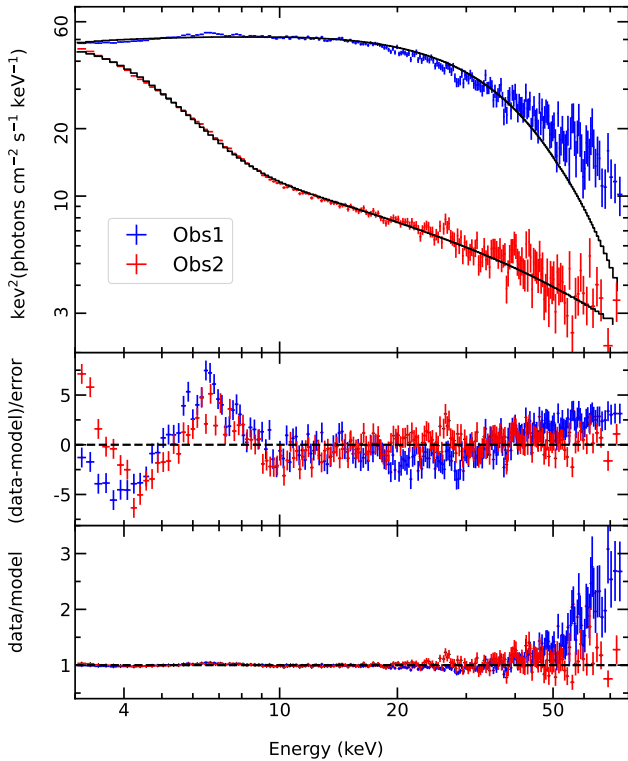


Figure 3. Upper panel: NuSTAR/FPMA spectral data in the HIMS (blue), the SIMS (red), and the fitted model `tbabs*(thcomp*diskbb)` (black solid line). Middle panel: data residuals with respect to the fitted model. Lower panel: data-to-model ratio. The presence of a prominent Fe K_α line and a weak reflection hump is seen.

low-mass BHXRBs GX 339–4 (Chand et al. 2024) and AT2019wey (Sahu et al. 2025) has also been reported by our group. A similar behavior is observed in the LHS of MAXI J1820+070, indicating that multiple Comptonization regions are required in the hard states of BHXRBs (Zdziarski et al. 2021a,c).

We then removed `ireflect` and `gaussian` components and adopted a more physically motivated model `relxillCp`, which is a part of the family of relativistic blurred reflection models `relxill` (Dauser et al. 2014; García et al. 2014). The `relxillCp` model self-consistently computes the reflection spectrum arising from the irradiation of thermally Comptonized coronal emission from the disk and also includes relativistic effects due to strong gravity near the black hole. The shape of the incident radiation in `relxillCp` is the same as in the `nthcomp` model. In `relxillCp`, we fixed the black hole spin at the maximum value of 0.998 and disk inclination angle at 40° (Peng et al. 2024; Svoboda et al. 2024). The outer disk radius was fixed at $1000 r_g$, and a single emissivity profile ($\propto r^{-q}$, q being

the emissivity index) was considered throughout the whole disk with q fixed at the canonical value of 3. The photon index (Γ) and electron temperature (kT_e) were varied independently of those in `thcomp`. Other free parameters of `relxillCp` were the inner disk radius (R_{in}), log of disk ionization ($\log \xi$), iron abundance (A_{Fe}), log of disk density ($\log N$), reflection fraction (R_{ref}), and normalization. To avoid the over prediction of the contribution of the reflection at lower energies, we multiplied `relxillCp` with a `mbknp` component, which helps to put a break on the reflection spectrum below a certain energy, and thus preventing the unphysical runaway of the photon spectrum at low energies (Steiner et al. 2024; Svoboda et al. 2024). The `mbknp` component is parameterized with the break energy B and index I , used for the correction for energies $E < B$. We set these parameters following the prescription outlined by Svoboda et al. (2024). This composite model, `plabs*tbabs(thcomp*diskbb+mbknp*relxillCp)` (hereafter M1), resulted in a significantly improved fit with $\chi^2/dof = 457.3/590$. The best-fit spectral parameters are listed in Table 2, and the corresponding spectral models and data are shown in Figure 4.

The results from our model M1 clearly indicate that the broadband spectrum in the 0.7–78 keV band in the HIMS requires two separate Comptonizing regions. The `relxillCp` component represents the hard Comptonizing region with $\Gamma \sim 1.8$ and $kT_e \sim 16$ keV, likely having a spherically extended geometry. This region is primarily responsible for the origin of the reflection features at a distant part of the disk. On the other hand, the second Comptonizing region, described by `thcomp`, is found to have low electron temperature, $kT_e \sim 4$ keV, and exhibits a relatively steeper spectrum with $\Gamma \sim 1.95$. This soft Comptonizing region may appear as a warm layer over the inner parts of the accretion disk. We also explored the possibility of an additional contribution to the reflection from the soft Comptonizing region by incorporating a second `relxillCp` as a reflection component only. However, we did not find any significant improvement in our spectral fitting. This implies that the reflection associated with the soft Comptonizing region is negligible, and the overall reflection spectrum is dominantly governed by the hard Comptonizing region.

The above model could not constrain the inner disk radius, R_{in} , properly. However, the lower bound at the 90% confidence level indicates that the disk is truncated away from the ISCO by at least $\sim 33 r_g$ (where $r_g = GM/c^2$ is the Gravitational radius). We also calculated the inner disk radius from the best-fit value of the `diskbb` normalization following its definition in XSPEC and considering the color correction factor of

1.7 (Shimura & Takahara 1995). The estimated radius is found to be $\sim 29 r_g$, which agrees closely with the obtained value from the reflection modeling. Furthermore, the temperature of the inner accretion disk is found to be ~ 0.4 keV, which is typically higher than that observed in the LHS. The disk appears to be highly ionized with slightly elevated density. Within the uncertainties, the iron abundance is consistent with the solar value. Additionally, the reflection fraction, R_{ref} , defined as the ratio of the coronal emission reaching the disk and the observer, is found to be ~ 0.64 , which in turn also favors the disk truncation scenario. All the best-fit spectral parameters indicate that the source was in HIMS during Obs1.

We then modeled the hard Comptonization spectra with the **compps** (Poutanen & Svensson 1996) model by replacing **relxillCp** in M1. The Comptonization model **compps** can treat the electron distribution in a corona as purely thermal, purely non-thermal, or hybrid for different shapes of the coronal geometry. Here, we assumed the electron distribution in the corona as purely thermal and the coronal geometry as spherical (**geom=0**) in the **compps** model. We also tested other geometries of the corona but did not notice any significant change in the spectral fitting. Therefore, we kept the geometry spherical, which also provides a relatively faster method for fitting the spectra than with the other geometries. In the **compps**, the seed photons for the Comptonization are considered to be multi-color disk photons provided by the **diskbb** component. We fixed the disk inclination angle at 40° and iron abundance at solar. The other free parameters of this model component are the electron temperature, kT_e , and the optical depth, τ , of the scattering medium. Furthermore, to account for the reflection from the disk, we convolved the **xilconv** model with both the Comptonizing regions. The reflection fraction, R_{refl} , and log of disk ionization, $\log \xi$, parameters in **compps** were allowed to vary freely. We kept the iron abundance fixed at solar, consistent with the value obtained from the model M1 within the uncertainty level. We also incorporated the **relconv** model to treat the relativistic blurring effects, while keeping the relevant parameters the same as those used for **relxillCp** in model M1. This model, **plabs*tbabs*relconv*xilconv*(thcomp*diskbb+compps)** (referred to as M2), provides a statistically acceptable fit to the broadband spectrum, with $\chi^2/dof = 458.7/592$. The best-fit spectral parameters are given in Table 2, and the best-fit spectra along with model components are shown in Figure 4.

We find that the optical depth (τ) of the hard Comptonizing region is ~ 9.7 . The accretion disk appears to

be highly ionized, and the relativistic reflection fraction (R_{ref}) is measured to be ~ 0.2 , which is slightly lower than the value obtained with model M1. This reduction may result from the inclusion of reflection contributions from both Comptonizing regions in the current model, which could dilute the apparent strength of the relativistic reflection component relative to that in model M1. Similar to our model M1, the lower bound on the inner disk radius at 90% confidence level suggests that the disk is truncated away from the ISCO by at least $43 r_g$. Besides, the other best-fit spectral parameters from M2 are in good agreement with those derived from M1.

In the next scenario, we incorporated spectral data from the HE and CZTI instruments onboard Insight-HXMT and AstroSat, respectively, to achieve broadband spectral coverage up to 200 keV. We first checked for any calibration uncertainties present in these data sets by fitting them up to 78 keV along with NICER and NuSTAR spectra data with both models M1 and M2. The resulting best-fit spectral parameters were either the same or well consistent with those found from the joint spectral fitting of NICER and NuSTAR spectral data in the 0.7 – 78 keV band using models M1 and M2, indicating no significant cross-calibration discrepancies among the instruments. Furthermore, inspection of the HE spectral data confirms that the background is significantly lower than the source rate in the 100 – 150 keV band. Based on the source and background count rates and their statistical uncertainties, we estimate a detection significance of $\sim 52\sigma$ for the source emission in the 100 – 150 keV band. We then extended the energy ranges of the HE and CZTI spectral data to 150 keV and 200 keV, respectively. However, we find that both models M1 and M2 were unable to describe the broadband spectra up to 200 keV, and provided poor spectral fits with $\chi^2/dof = 803/679$ for M1 and $886.8/682$ for M2, leaving a prominent hump at high energies ($\gtrsim 100$ keV). Figure 5 presents the broadband spectral data in the 0.7 – 200 keV band fitted with the model M2, along with the residuals, highlighting the deviations between the observed data and the model.

The clear excess at $\gtrsim 100$ keV further suggests that the models with thermal Comptonization and disk reflection alone are insufficient to explain the high-energy emission, and may originate due to the presence of a power-law tail originating in the non-thermal distribution of hot electrons in the corona. We then tried to model this power-law tail by invoking a hybrid Comptonization scenario within the **compps** framework, wherein the Lorentz factor (γ_{min}) defines the transition point from a thermal to a power-law electron distribution. We allowed γ_{min} to vary freely while fixing

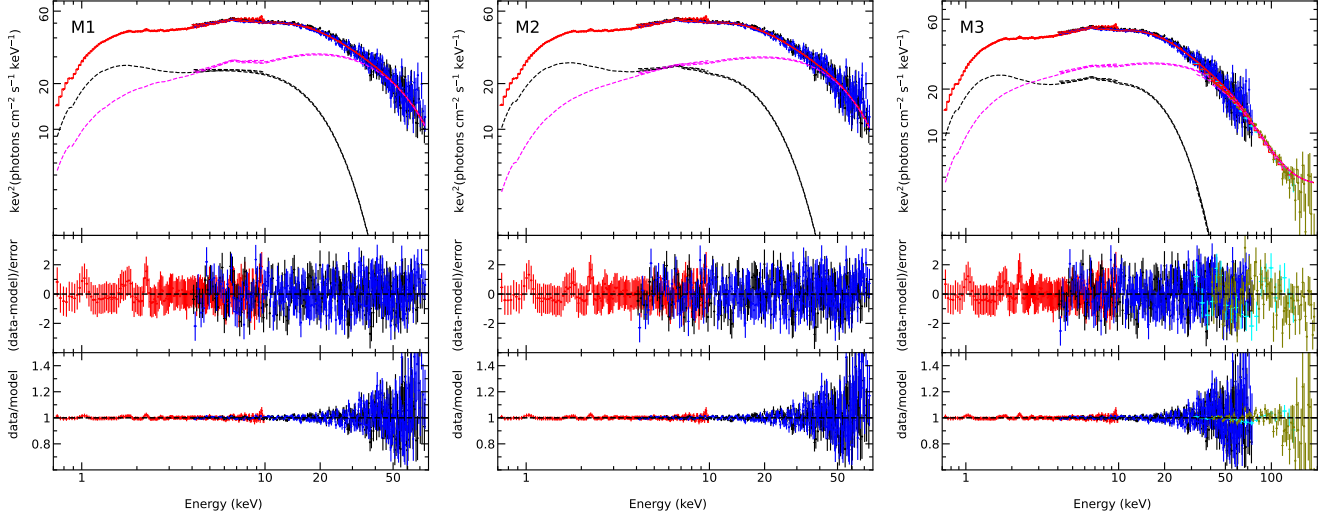


Figure 4. Joint NICER (red), NUSTAR/FPMA (black), and FPMB (blue) spectral data in the HIMS along with the best-fit models M1: `plabs*tbabs(thcomp*diskbb+mbknpo*relxillCp)` (left panel), and M2: `plabs*tbabs*relconv*xilconv(thcomp*diskbb+compps[thermal])` (middle panel). The right panel shows the joint NICER, NuSTAR/FPMA, FPMB, HE (cyan), and CZTI (olive) spectral data along with the best-fit model M3: `plabs*tbabs*relconv*xilconv(thcomp*diskbb+compps[hybrid])`. The black dotted line indicates the `thcomp` convolved with `diskbb` component, whereas the magenta dotted line represents the `relxillCp` for M1, and `relconv` and `xilconv` components convolved with `compps` components for M2 and M3.

$\gamma_{\max} = 1000$ and keeping the electron power-law index fixed at 2. This model, referred to as M3, which assumes a hybrid electron distribution with Maxwellian and non-thermal above a certain value of γ_{\min} , provides a very good and significantly improved spectral fit in the 0.7 – 200 keV band with $\chi^2/\text{dof} = 601.5/681$ with $\Delta\chi^2 \approx -285$ for 1 dof. The best-fit spectral parameters obtained from M3 are listed in Table 2, and the best-fit spectral data with the model components are shown in Figure 4. We find γ_{\min} to be ~ 1.33 , implying a significant contribution from the non-thermal distribution. The other best-fit spectral parameters obtained with model M3 agree closely with those obtained from our earlier models, assuming a purely thermal electron distribution up to 78 keV.

3.1.2. SIMS

For Obs2, we performed a joint spectral analysis using contemporaneous NICER and NuSTAR data in the 0.8–78 keV band. The NICER data below 0.8 keV were discarded to avoid calibration uncertainties. These observations were taken during the decay phase of the 2023 outburst. Residuals from fitting the NuSTAR/FPMA spectral data with the model `tbabs(thcomp*diskbb)` revealed a moderately broad Fe K α line and a weak reflection hump (see Figure 3). We initiated the joint fitting by including a `plabs` component to account for calibration uncertainties, a `gaussian` component to model the iron line, and the

`ireflect` component convolved with `thcomp` to account for reflection from ionized material. Our current model `plabs*tbabs(ireflect*thcomp*diskbb+gaussian)` provided a poor spectral fit with $\chi^2/\text{dof} = 826.2/523$. We also noticed that replacing `thcomp` with `cutoffpl` resulted in a marginally improved fit, though the overall fit quality remained unsatisfactory. Despite the poor spectral fits, relatively higher inner disk temperature, kT_{in} , and steeper photon index, Γ , suggest that the source might have gradually transitioned to the SIMS between Obs1 and Obs2.

We then employed the more physically motivated and relativistically blurred reflection model, `relxillCp`, to perform broadband reflection spectroscopy, replacing the `ireflect` and `gaussian` components. Here, `relxillCp` is considered only as a reflection component by fixing the reflection fraction parameter at -1 . The common parameters such as Γ and kT_e were tied between the `relxillCp` and `thcomp` components. The inclination angle and the iron abundance were also kept fixed at 40° and solar, respectively. Other free spectral parameters of the `relxillCp` model are the emissivity index (q), log of disk ionization ($\log \xi$), log of disk density ($\log \rho$), and normalization. Additionally, we varied the black hole spin (a) and inner disk radius (R_{in}) freely, considering the SIMS. The resulting model `plabs*tbabs(thcomp*diskbb+relxillCp)` (now referred to as M4) provides a good and statistically acceptable fit with $\chi^2/\text{dof} = 506.5/521$. This further sug-

Table 3. Best-fit broadband X-ray spectral parameters derived for Obs2 (SIMS)

Component	Parameter	M4	M5	M6
TBabs	$N_{\text{H}} (10^{22} \text{ cm}^{-2})$	0.26 ± 0.01	0.28 ± 0.01	0.31 ± 0.01
Diskbb	$kT_{\text{in}} \text{ (keV)}$	0.87 ± 0.01
	norm ($\times 10^3$)	$9.5^{+1.4}_{-0.8}$
Thcomp	Γ	2.36 ± 0.03	$2.33^{+0.06}_{-0.03}$	2.35 ± 0.04
	$kT_{\text{e}} \text{ (keV)}$	$998.2_{-500.4}$	$462.5_{-382.3}$	$1000_{-505.8}$
	C_{f}	$0.25^{+0.04}_{-0.06}$	0.2 ± 0.1	$0.23^{+0.06}_{-0.1}$
Kerrbb	a	...	$0.79^{+0.03}_{-0.13}$...
	i°	...	$46.6^{+3.2}_{-4.7}$...
	$\dot{M} (\times 10^{18} \text{ g/s})$...	1.52 ± 0.08	...
	$M_{\text{BH}} (M_\odot)$...	$10.5^{+7.7}_{-3.0}$...
	$D \text{ (kpc)}$...	$3.5^{+1.3}_{-0.5}$...
BHSPEC [$\alpha = 0.1$]	$M_{\text{BH}} (M_\odot)$	$19.5^{+1.4}_{-6.0}$
	L/L_{Edd}	$0.19^{+0.03}_{-0.10}$
	a	$0.8_{-0.08}$
	i°	$47.4^{+2.7}_{-5.0}$
	$D \text{ (kpc)}$	$6.0_{-0.8}$
RelxillCp (refl. only)	a	$0.98_{-0.29}$
	i°	40^f
	$R_{\text{in}} (r_{\text{isco}})$	$1.7^{+0.9}$	1^f	1^f
	q	$3.7^{+0.6}_{-0.4}$	$6.55_{-2.99}$	$6.14^{+2.8}_{-2.2}$
	$\log \xi$	$4.09^{+0.04}_{-0.11}$	$4.27^{+0.13}_{-0.25}$	$4.20^{+0.07}_{-0.12}$
	$A_{\text{Fe}} \text{ (solar)}$	1^f	1^f	1^f
	$\log N$	17^f	$17.0^{+1.3}_{-0.2}$	17^f
	norm	$0.19^{+0.01}_{-0.02}$	$0.19^{+0.02}_{-0.05}$	$0.21^{+0.02}_{-0.03}$
mbknp0	B	1.57 ± 0.07	1.66 ± 0.08	$1.55^{+0.07}_{-0.09}$
	I	0.8^f	0.8^f	0.8^f
Flux _{0.001–500 keV} ^{unabs} [$10^{-7} \text{ erg cm}^{-2} \text{ s}^{-1}$]		~ 2.5	~ 2.5	~ 2.6
Cross-calibration	$\Delta\Gamma_{\text{NICER}}$	0.13 ± 0.01	0.14 ± 0.01	0.13 ± 0.01
	K_{NICER}	0.82 ± 0.02	0.81 ± 0.02	0.81 ± 0.02
	$\Delta\Gamma_{\text{NuSTAR B}}$	$0.002^{+0.006}$	$0.003^{+0.006}$	$0.002^{+0.006}$
	$K_{\text{NuSTAR B}}$	0.98 ± 0.01	0.98 ± 0.01	0.98 ± 0.01
χ^2/dof		506.5/521	470.9/519	486.8/520

Note. M4: `plabs*tbabs(thcomp*diskbb+mbknp0*relxillCp)`, M5: `plabs*tbabs(thcomp*kerrbb+mbknp0*relxillCp)`, M6: `plabs*tbabs(thcomp*bhspec+mbknp0*relxillCp)`. ^f – indicates fixed parameters.

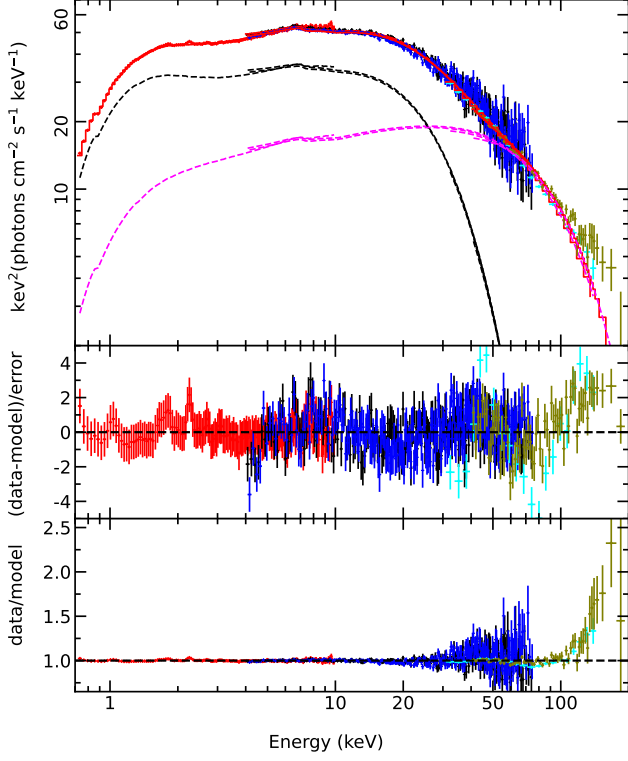


Figure 5. Upper panel: NICER (red), NUSTAR/FPMA (black), FPMB (blue), HE (cyan), and CZTI (olive) spectral data in the HIMS along with the fitted model M2, which considers only a Maxwellian distribution of the electrons in the corona. Middle and lower panels: deviations of jointly fitted NICER (red), NuSTAR/FPMA (black) and FPMB (blue), HE (cyan), and CZTI (olive) spectral data from the model M2. The black and magenta dotted lines have the same meaning as in Figure 4 for model M2. A prominent excess above 100 keV is observed. The data is rebinned for plotting purposes only.

gests that a model consisting of a single Comptonizing region, its associated reflection, and disk emission is sufficient to describe the 0.8–78 keV spectrum in the SIMS, unlike the HIMS, where two distinct Comptonizing regions were required. The best-fit spectral parameters obtained from M4 are listed in Table 3, and the corresponding spectral data and models are shown in Figure 6.

The Galactic absorption column density, N_{H} , is found to be $\sim 0.26 \times 10^{22} \text{ cm}^{-2}$. The best-fit values of kT_{in} and Γ indicate that the inner accretion disk has become significantly hotter (~ 0.9 keV), and the continuum has steepened, consistent with the source being in the SIMS. The electron temperature, kT_{e} , could not be constrained, likely due to the absence of a clear high-energy cutoff. Compared to the HIMS, the inner disk radius has decreased substantially, reaching close to the

ISCO with $R_{\text{in}} \lesssim 2.6 R_{\text{isco}}$. Additionally, the estimated radius of $\sim 7 - 8 r_{\text{g}}$ from the `diskbb` normalization following the similar procedure adopted in the HIMS also suggests a relatively closer extent of the disk. The disk ionization parameter is also found to be higher than that in the HIMS. As the disk density could not be constrained, it was fixed at its best-fit value of 10^{17} cm^{-3} , which is slightly higher than the value inferred during the HIMS. These spectral parameters together suggest that the source transitioned to the SIMS during Obs2.

We next replaced the `diskbb` component with the relativistic disk model `kerrbb` (Li et al. 2005), which describes a geometrically thin, steady-state accretion disk around a Kerr black hole. The inner disk radius was fixed at the ISCO, and a zero-torque boundary condition was assumed at the inner edge. The spectral hardening factor was set to the canonical value of 1.7 (Shimura & Takahara 1995), and disk self-irradiation was included. The black hole spin, a , and disk inclination angle, i , were tied between the `kerrbb` and `relxillCp` components and allowed to vary. Other free parameters of `kerrbb` are the mass accretion rate (\dot{M}), mass of the black hole (M_{BH}), and distance to the source (D). This model, `plabs*tbabs(thcomp*kerrbb+relxillCp)` (now referred to as M5), provides a better fit compared to the previous model M4, with $\chi^2/\text{dof} = 470.9/519$. The best-fit spectral parameters are given in Table 3, and the corresponding spectral data with the best-fit model is shown in Figure 6.

We obtain the best-fit black hole spin, $a = 0.79^{+0.03}_{-0.13}$, mass, $M_{\text{BH}} = 10.45^{+7.7}_{-3.0} M_{\odot}$, and disk inclination angle, $i = 46.6^{+3.2}_{-4.7}$. We also estimated the black hole mass using the mass function proposed by Mata Sánchez et al. (2025), defined as $f \equiv M_1 \sin^3 i / (1 + M_2/M_1)^2 = 2.77 \pm 0.09 M_{\odot}$, where M_1 and M_2 denote the masses of the black hole and the donor star, respectively. For this, we adopted the value of inclination angle, i , from this model M5 and considered M_2 varying between 0.2–0.78 M_{\odot} (Mata Sánchez et al. 2025; Zdziarski et al. 2025b). The black hole mass estimated from the mass function lies in the range $\sim 7.8 - 9.4 M_{\odot}$. In addition, the derived value of the distance to the source obtained from this model is $D = 3.47^{+1.32}_{-0.49}$ kpc. Furthermore, the inferred value of the mass accretion rate, $\dot{M} = 1.52 \pm 0.08$ g/s, corresponds to the luminosity of $\sim 0.1 L_{\text{Edd}}$, assuming a black hole mass of $M_{\text{BH}} = 10 M_{\odot}$. The other best-fit spectral parameters, including Γ , kT_{e} , $\log \xi$, and $\log N$, from the model M5 are well consistent with those estimated from the previous model M4.

In our next model, we used another relativistic disk model `bhspec` to model the thermal emission from the disk by replacing `kerrbb` in M5. Like `kerrbb`, the inner

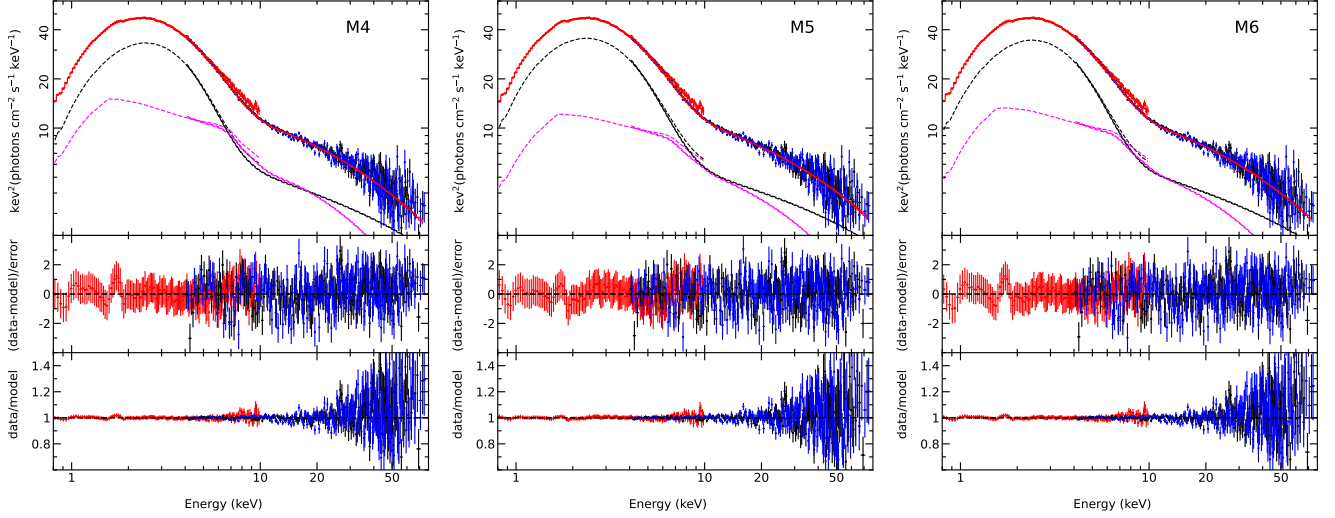


Figure 6. Joint NICER (red), NUSTAR/FPMA (black), and FPMB (blue) spectral data of the SIMS observations along with best-fit model M4: `plabs*tbabs(thcomp*diskbb+mbknp*relxillCp)`, M5: `plabs*tbabs(thcomp*kerrbb+mbknp*relxillCp)`, and M6: `plabs*tbabs(thcomp*bhspec+mbknp*relxillCp)`. The black dotted line represents the `thcomp` component convolved with `diskbb` for M4, `kerrbb` for M5, and `bhspec` for M6, whereas the magenta dotted line shows the `relxillCp` (reflection only) component.

disk is assumed to extend down to the ISCO in `bhspec`. The primary difference between these two relativistic disk models lies in the treatment of disk emission. While `kerrbb` considers a color-corrected blackbody approximation, `bhspec` employs detailed atmospheric-like calculations for each disk annulus to calculate the vertical disk structure and radiative transfer processes self-consistently (Davis et al. 2005; Davis & Hubeny 2006). `bhspec` is available as two table models for different values of the viscosity parameter, α , of 0.01 and 0.1 that consider the black hole spin parameter in the range of $0 - 0.99$ and $0 - 0.8$, respectively. Since $\alpha = 0.1$ is more appropriate for BHXBs, we adopted the second table model even though it allows a smaller range of black hole spin. The black hole spin (a) and disk inclination angle (i) were tied between `bhspec` and `relxillCp`, and allowed to vary. The other free parameters of `bhspec` are black hole mass (M_{BH}), and luminosity of the accretion disk (L/L_{Edd}). We varied the `bhspec` normalization, defined as $(10 \text{ kpc}/D)^2$ (where D is the source distance), over a range corresponding to source distances between 2 and 6 kpc. This model `plabs*tbabs(thcomp*bhspec+relxillCp)` (referred to as M6) provided a good and statistically acceptable fit with $\chi^2/\text{dof} = 486.8/520$. The best-fit spectral parameters are listed in Table 3, and the spectra, along with the best-fit model, are shown in Figure 6. We find a black hole mass of $M_{\text{BH}} = 19.5^{+1.4}_{-6.0} M_{\odot}$ and a poorly constrained source distance of $D = 6.0_{-0.8} \text{ kpc}$. The obtained values of disk luminosity and inclination angle are

found to agree with those inferred from M5 within the error bars. Other best-fit spectral parameters also appear to be broadly consistent with those obtained from the models M4 and M5.

3.2. Timing Analysis

To investigate the source variability, we extracted PDSs across multiple energy bands during both the HIMS and SIMS. In the HIMS, we obtained white-noise subtracted and rms-normalized PDSs in the 0.5–2 keV and 5–10 keV bands from NICER data, and in the 30–50 keV, 50–80 keV, and 80–120 keV bands from HXMT/HE data using the `powspec` task of the XRONOS package. For HXMT/HE data, the background-subtracted lightcurves were used to derive the PDSs. Additionally, we derived cross power density spectra (CPDSs) in the 10–30 keV band from NuSTAR observations using the HENDRICS package (Bachetti et al. 2015), combining the two focal plane modules and subtracting the white noise contribution. The CPDS method involves performing Fourier transforms of two simultaneous light curves from the `fpma` and `fpmb` modules and computing their complex cross-spectrum (cospectrum). The real part of this cospectrum serves as a good alternative to a white-noise-subtracted PDS, as it effectively suppresses uncorrelated Poisson noise and properly handles data gaps (see Bachetti et al. 2015, for a detailed description). AstroSat/CZTI data were excluded from the timing analysis due to their low signal-to-noise ratio, likely resulting from the relatively small effective area and limited sensitivity of the instrument (Singh et al. 2025). In

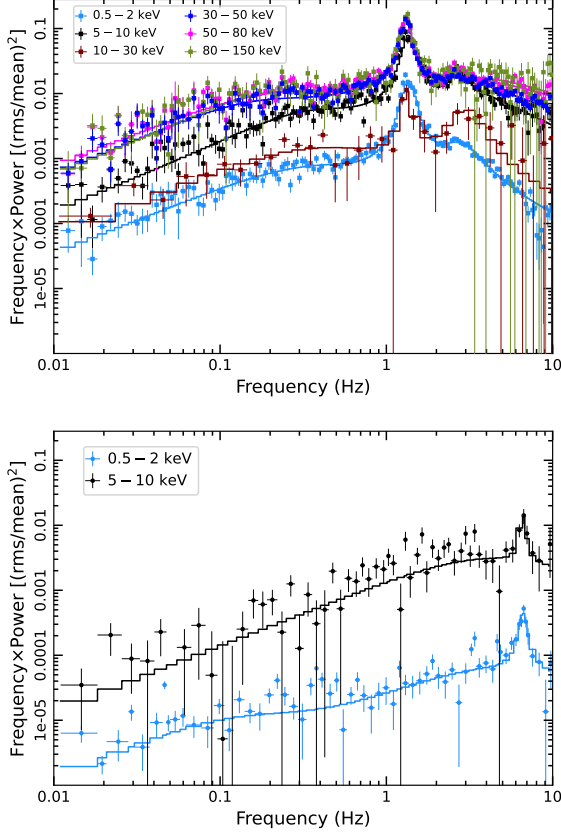


Figure 7. Upper panel: PDSs from the NICER, and Insight-HXMT/HE observations, and CPDS from the NuSTAR observation derived in different energy bands during the HIMS. Lower panel: PDSs from the NICER observation derived in two different energy bands during the SIMS. Some of the PDSs are rebinned for plotting purposes only.

the SIMS, PDSs were derived only from NICER data in the 0.5–2 keV and 5–10 keV bands. The PDSs and CPDS corresponding to both spectral states are presented in Figure 7.

During the HIMS, the power of the PDS at soft energies is lower across all frequencies, increasing gradually with energy and then saturating beyond ~ 30 keV. Notably, the CPDS in the 10–30 keV band derived from the NuSTAR observation shows relatively lower power than the PDS in the 5–10 keV band, which could be due to the effect of dead-time in the NuSTAR detectors. Regardless of the energy ranges, a clear presence of a QPO at ~ 1.3 Hz accompanied by an upper-harmonic at ~ 2.7 Hz is observed in all the PDSs and CPDS in the HIMS. A similar presence of a QPO along with upper-harmonic using AstroSat/LAXPC data in the HIMS of this source was also reported by Nandi et al. (2024). In the SIMS, the overall shape of the PDSs remains similar. However, the QPO frequency has now shifted to a

relatively higher frequency of ~ 6.6 Hz, and any prominent signature of the presence of the upper-harmonic up to 10 Hz was not noticed. The energy-dependent behavior of the PDSs across both spectral states indicates that the low-energy photons, primarily originating from the disk, exhibit significantly lower variability compared to the higher-energy photons, which are dominated by coronal emission.

We also investigated fractional rms variability amplitude as a function of photon energy for the 0.01–10 Hz frequency range using both the observations in the HIMS and SIMS. For the HIMS, we derived the rms-energy spectra over the 0.5–120 keV band using data from NICER, NuSTAR, and HXMT/HE, whereas NICER and NuSTAR data were employed in the SIMS to derive the rms-energy spectrum in the 0.5–30 keV band. We utilized the spectral and timing analysis package *Stingray* (Huppenkothen et al. 2019a,b) to derive the rms-energy spectra from NICER data. For the NuSTAR and HXMT/HE data, we first extracted CPDSs and PDSs at different energy bands and then calculated the fractional rms for the 0.01–10 Hz frequency range from each CPDS and PDS. The rms-energy spectra in two distinct spectral states are shown in Figure 8. In both the HIMS and SIMS, the fractional rms variability amplitude appears to be low ($\sim 5\%$) at soft energies, dominated by the thermal disk emission, and gradually increases up to ~ 30 – 40% at hard energies, where the coronal emission dominates. We note that the NuSTAR data demonstrate significantly lower variability than the NICER data around the same energy bins, which is likely due to the effect of dead time in the NuSTAR detectors, reducing the variability amplitude artificially (M. Bachetti, private communication; Bachetti & Huppenkothen 2018; Zdziarski et al. 2024b). It is worth noting that the effects of dead time are significant for bright sources, but become progressively less pronounced for sources of lower intensity. The non-constant and very long (~ 2.5 ms) nature of the NuSTAR dead time further complicates its accurate correction (Bachetti & Huppenkothen 2018). To further investigate this effect, we used the HXMT/ME data that has a substantial overlap with the NuSTAR data within a certain energy range. We found that the fractional rms derived from the HXMT/ME data is significantly higher than those from the NuSTAR data, and closely matches the measurements from the NICER data. This further confirms that the low rms in the NuSTAR data is due to the effect of the dead time.

4. DISCUSSIONS

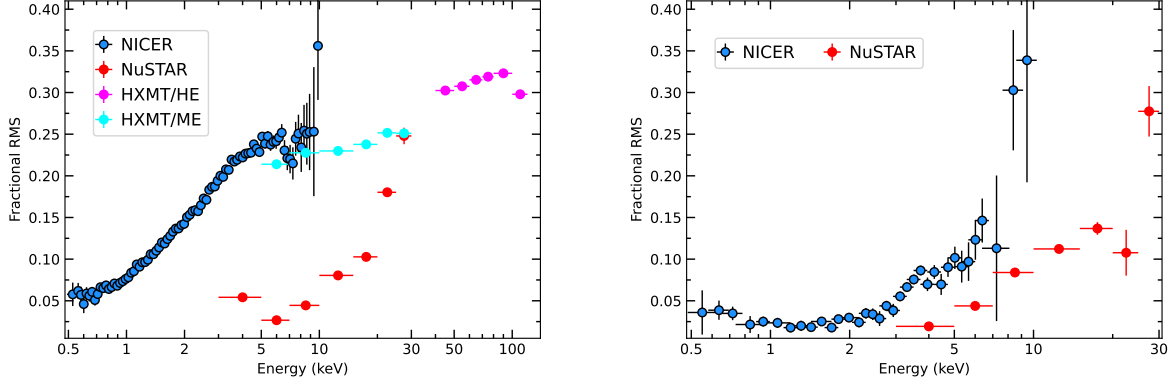


Figure 8. Fractional rms as a function of photon energy for the 0.01-10 Hz range in the HIMS (left panel) and the SIMS (right panel). The blue, red, cyan, and magenta circles represent the NICER, NuSTAR, HXMT/ME, and HXMT/HE observations, respectively.

We have performed a broadband spectral study of the newly detected Galactic BHXR Swift J1727.8–1613 during its 2023 outburst over the 0.7 – 200 keV band in the HIMS using simultaneous NICER, NuSTAR, Insight-HXMT/HE, and AstroSat/CZTI observations, and over the 0.7 – 78 keV band in the SIMS using contemporaneous observations from NICER and NuSTAR data. We also investigate the source variability across the two different spectral states. This outburst is found to be a complete one, similar to the canonical outbursts seen in low-mass BHXBs. Substantial evolution in the spectral hardness also indicates a spectral state transition from the HIMS to the SIMS between the two observations.

4.1. Thermal Comptonization and Accretion Disk

The analysis of the NuSTAR/FPMA spectral data reveals that the reflection component was notably weak during both observations (see Figure 3). Although residuals from both observations exhibit a distinct feature in the 6–7 keV band, indicative of an iron emission line, the characteristic reflection hump, typically peaking in the 20–40 keV band, was either faint or absent. Additionally, an upward trend in the residuals above ~ 50 keV was observed during the HIMS but was not present during the SIMS. A similar high-energy excess above 40 keV, along with a weak reflection hump, was previously reported in NuSTAR and Insight-HXMT observations during the LHS by Liu et al. (2024). The authors found the reflection hump in the Insight-HXMT data to be relatively prominent, peaking around 20 keV. They proposed that this feature may be partially artificial, resulting from an improper modeling of the high-energy rollover by the `cutoffpl` model used in their spectral analysis.

Our spectral analysis in the 0.7–78 keV band during the HIMS reveals that the broadband spectrum requires

models comprising thermal Comptonization of the disk photons in two physically distinct Comptonizing regions, their associated reflections, and thermal emission from the disk. The reflection due to the hard component originates from a distant part of the disk, where relativistic effects are weak, and strong illumination is observed. On the other hand, the reflection from the soft component, dominating at low energies, appears to be more blurred due to its proximity to the inner disk. Polarimetric studies of the source also favor radially extended coronal geometry confined to the disk plane, rather than being aligned along the jet axis (Ingram et al. 2024; Velezina et al. 2023).

We do not find any evidence for a high-energy tail, typically associated with Comptonization by non-thermal scattering electrons in the corona, up to 78 keV. It is worth mentioning here that Liu et al. (2024) attributed the excess above 40 keV observed in the LHS to the presence of a high-energy tail extending beyond the thermal Comptonization component. Moreover, Peng et al. (2024) also suggested the excess above 40 keV in the NuSTAR and Insight-HXMT spectral data taken in the transitioning period of the source towards the HIMS arises due to the presence of a hard X-ray tail coming from either a relativistic jet or from the base/corona below a slowly moving jet. The authors used a single Comptonizing region and a cutoff power-law model to account for the hard X-ray tail. However, a similar upward trend above ~ 50 keV (see Figure 3), observed in this work, is well reproduced by adopting a model that includes two thermal Comptonizing regions.

Results from the reflection modeling suggest that the inner edge of the accretion disk is truncated well away from the ISCO. Although we are able to place a lower bound on the inner disk radius (R_{in}), this parameter remains relatively insensitive to the specific choice of

the continuum model, preventing a definitive constraint on the degree of truncation. The lack of a prominent reflection hump makes it difficult to robustly estimate R_{in} through reflection spectroscopy. However, an independent measurement of $R_{\text{in}} \sim 29\text{--}35 r_{\text{g}}$ obtained from modeling the disk continuum also supports the scenario of a truncated accretion disk in the HIMS.

The precise location of the inner edge of the accretion disk in the LHS of BHXRBs remains an open and complex question. Using reflection modeling with `relxill` and framework of a single Comptonizing region, Liu et al. (2024) reported that the accretion disk in Swift J1727.8–1613 extends close to the ISCO during the LHS. However, their analysis required a super-solar iron abundance, which may be an artifact due to the fixed disk density at 10^{15} cm^{-3} in the `relxill` model (García et al. 2018; Jiang et al. 2019; Zdziarski et al. 2022). Additionally, they attributed the observed low reflection fraction to an outflowing plasma. Notably, the interpretation of the accretion disk extending close to the ISCO based on the detection of broad Fe $K\alpha$ line in the LHS (Miller et al. 2006, 2008) and the bright LHS (García et al. 2015, 2019) of a few BHXRBs has been challenged by adopting the framework of double Comptonizing regions (Zdziarski et al. 2021b,c, 2022; Banerjee et al. 2024; Chand et al. 2024). In such scenarios, the apparent broadening of the iron line (even at the bright LHS with $L \approx 2 - 15\% L_{\text{Edd}}$) may result from the Compton scattering of the reflected photons within a soft, optically thick Comptonizing region overlaying the disk, rather than the relativistic effect. In addition, Mahmoud & Done (2018) showed, using their spectral-timing model including Fourier-resolved spectroscopy, that two distinct Comptonizing regions with a stratified corona are required to describe the shape of the broadband spectra, variability, and energy-dependent lags in the bright LHS of Cyg X-1. Moreover, Mahmoud et al. (2019) demonstrated that the long reverberation lags observed in the LHS of BHXRBs cannot be explained by considering a single homogeneous Comptonizing medium with the accretion disk extending close to the ISCO. Their results suggest that a model with two separate Comptonizing regions and a substantially truncated accretion disk is necessary to account for the long reverberation lags.

The moderate to high disk ionization inferred from our analysis is likely due to strong coronal illumination. However, the relatively high intrinsic disk temperature ($\sim 0.4 \text{ keV}$) may also contribute significantly to the elevated ionization state. The covering fraction ($C_{\text{frac}} \sim 0.4$) suggests that a substantial portion of the disk photons are intercepted by the soft

Comptonizing region, further supporting its interpretation as a warm, optically thick layer enveloping the disk. The overall spectral characteristics observed in the HIMS of Swift J1727.8–1613 closely resemble the broadband (0.7–100 keV) spectrum of the low-mass BHXRB GX 339–4 in the same state (Chand et al. 2024).

4.2. Hybrid Comptonization

We notice that Comptonization by a purely thermal electron population fails to describe the high-energy excess at $\gtrsim 100 \text{ keV}$ (see Figure 5); instead, a hybrid electron distribution is required. In particular, $\gamma_{\text{min}} \sim 1.3$, with electron power-law index of 2, suggests that a significant portion of the high-energy emission arises from inverse Compton scattering of soft photons by the non-thermally distributed electrons. This provides strong evidence for a hybrid coronal plasma, where thermal electrons dominate the Comptonized spectrum at low energies, with a non-thermal tail emerging above a certain energy due to the non-thermally populated electrons. This hybrid model also favors the scenario where the disk is truncated far away from the ISCO, consistent with the presence of non-thermal particle acceleration within a hot and optically thin inner accretion flow.

Evidence of the possible presence of a hard X-ray tail originating from non-thermal electrons in the LHS of Swift J1727.8–1613 during the same outburst was previously reported by Liu et al. (2024). Their results show that the contribution from the non-thermal electron population was relatively soft with a steeper distribution at the initial phase of the outburst, and the particle acceleration gradually increased as the source was transitioning towards the HIMS during the rising phase. This is consistent with our present results, where significant non-thermal particle acceleration is seen in the HIMS. Furthermore, hybrid Comptonization with a significant non-thermal electron population with $\gamma_{\text{min}} \sim 1.3$ and slightly steep electron power-law index of ~ 2.5 was also reported in the LHS of the bright low-mass BHXRB MAXI J1820+070 by Zdziarski et al. (2021c). This detection, along with a substantially truncated accretion disk in the LHS, was further confirmed in the follow-up study including Insight-HXMT data by Zdziarski et al. (2022).

The electron temperature, $kT_e \sim 13 - 18 \text{ keV}$, of the hard Comptonizing region, inferred from all three spectral models (M1-M3) in the HIMS, remains low, which could be a consequence of the energy balance within the accretion flow. Alternatively, such a low kT_e could also result from efficient cooling by synchrotron photons produced by a hybrid electron distribution (Zdziarski &

Gierliński 2004; Malzac & Belmont 2009; Veledina et al. 2011; Zdziarski et al. 2021c).

4.3. State Transition and Disk Evolution

In contrast to the HIMS, the coronal structure during Obs2 appears to be relatively simple and can be described with a single Comptonizing region. A relatively steeper photon index and a low covering fraction further indicate that the corona became weak in this state. We also notice a significant evolution in the accretion disk in terms of elevated inner disk temperature, ionization, and relatively closer extent (obtained from modeling both the reflection and disk continuum modeling) to the ISCO. These further suggest that the source transitioned to the SIMS during Obs2.

4.4. Spin, Mass, Distance, and Disk Inclination

Reflection modeling alone (see model M4) could not constrain the spin properly, yielding a value $\gtrsim 0.7$ at the 90% confidence limit. Peng et al. (2024) reported a very high black hole spin of $0.98^{+0.02}_{-0.07}$ for Swift J1727.8–1613 by modeling the reflection continuum in the LHS. However, the reflection method for spin measurement relies on the assumption that the disk extends down to the ISCO or very close to it, and the extent of the inner accretion disk in the LHS is highly debated. On the other hand, our spin estimation of $0.79^{+0.03}_{-0.13}$ by modeling the disk continuum and reflection component together (see model M5), which provides a more physically self-consistent approach, is slightly lower but broadly consistent with the value reported by Svoboda et al. (2024), using the HSS observations of the source in February 2024.

We find a close agreement between our estimated black hole mass, $M_{\text{BH}} = 10.5^{+7.7}_{-3.0} M_{\odot}$ (see model M5), and previously reported values. This value also appears to be consistent with the black hole mass obtained from the mass function suggested by Mata Sánchez et al. (2025). Furthermore, Zdziarski et al. (2025b) favored a black hole mass of $\lesssim 13 M_{\odot}$ for Swift J1727.8–1613, which aligns well with our estimate. Additionally, Debnath et al. (2025), using the propagating oscillatory shock model and the observed QPO–photon index correlation, reported a black hole mass of $\sim 13 M_{\odot}$ for this source that is also consistent with our results. Although the black hole mass inferred from *bhspec* appears to be consistent with that obtained from *kerrbb* within error bars, the slightly higher value is likely a consequence of the poorly constrained source distance in *bhspec*. It should be noted here that the *bhspec* model does not account for returning radiation, in which photons emitted from the inner disk are gravitationally bent back

onto the disk surface. This process can introduce additional heating and alter the observed thermal spectrum, particularly in the high-energy tail. The effect becomes significant for systems with high black hole spin and high inclination. Although the spin and inclination inferred in this work represent a moderately relativistic regime, the omission of returning radiation may still introduce a minor systematic uncertainty in the derived disk parameters using this model. However, our estimate of the source distance, $D = 3.5^{+1.3}_{-0.5}$ kpc, from the *kerrbb* component agrees well with the value reported by Mata Sánchez et al. (2025) based on the optical spectroscopy.

The disk inclination angle obtained from the models M5 and M6 lies in the range of 42° – 50° , which is in good agreement with the 30° – 50° range estimated by Svoboda et al. (2024) from polarimetric analysis of the HSS observation. Additionally, Peng et al. (2024) also reported a disk inclination angle of $\sim 40^{\circ}$ using LHS observations in 2023. However, some studies reported the disk inclination angle in Swift J1727.8–1613 to be $\gtrsim 78^{\circ}$ (Chatterjee et al. 2024; Debnath et al. 2024), which is unlikely given the absence of any eclipse or dips in the source lightcurve.

4.5. Source Variability

The shapes of the PDSs in different energy bands indicate a slight decrease in variability as the source transitioned to the SIMS. In both the spectral states, the increase in PDS power with energy suggests that high-energy coronal photons exhibit stronger variability than the softer ones, associated with the disk. In the HIMS, however, the PDSs above 30 keV are nearly identical, suggesting a similar variability pattern among hard photons in this energy range. Additionally, the significant increase in QPO frequency from ~ 1.3 Hz to ~ 6.6 Hz suggests a change in the disk–corona geometry between the two states. If QPOs are thought to be associated with the inner edge of the disk or the outer boundary of the inner hot flow, the observed increase in the QPO frequency implies that the disk has moved relatively closer to the ISCO in the SIMS, potentially accompanied by a contraction of the corona. This interpretation is consistent with the results from our spectral modeling, where the disk is found to be moving closer to the ISCO in the SIMS.

The shapes of the rms–energy spectra observed in the HIMS and SIMS differ from those reported by Gierliński & Zdziarski (2005) for the LHS of XTE J1650–500 using RXTE data, where the variability is stronger at lower energies and gradually decreases with increasing photon energy. However, their study lacked coverage below 3 keV, making it difficult to investigate the variabil-

ity associated with the disk emission at softer energies. The morphology of the rms-energy spectra does not always remain the same and is found to vary across the spectral states and sources as well. In the intermediate states of the BHXRB XTE J1550–564, [Gierliński & Zdziarski \(2005\)](#) reported that fractional rms increases with the increase in photon energy. This trend is consistent with our findings in both the HIMS and SIMS of Swift J1727.8–1613. In addition, a similar trend in the rms-energy spectrum derived at the QPO frequency was also reported during the HIMS of the low-mass BHXRB MAXI J1803–298 by [Chand et al. \(2022\)](#), though their study also lacked the data below 3 keV.

Our investigation of the rms-energy spectra in both the spectral states reveals a weakly variable or stable disk and a highly variable power-law component, mainly governing the overall source variability. The nature of the variability remains similar between the two states, though a slight decrease is observed in the SIMS. Since our data in the HIMS is limited only up to 120 keV, and our spectral modeling suggests that the contribution from non-thermal distribution becomes significant above ~ 100 keV, a robust statement on the variability associated with the non-thermal electron population is difficult. Moreover, the lack of high-energy data in the SIMS also restricts us from studying the variability pattern governed by the high-energy photons (> 30 keV), and the non-thermal electron population in this state.

5. CONCLUSIONS

Our main results from this study are as follows.

The broadband spectrum up to 78 keV in the HIMS can be described with models having two different Comptonizing regions, with the electron distribution being predominantly thermal or Maxwellian. We did not notice any contribution from the non-thermal electron population in the spectral data up to 78 keV in the HIMS. The disk-corona geometry of Swift J1727.8–1613 shows strong similarity with that of GX 339–4 in the HIMS ([Chand et al. 2024](#)).

The contributions from the non-thermal electron distribution become significant above 100 keV, where a weak hard X-ray tail is observed. The shape of this tail can be satisfactorily described considering a hybrid electron distribution in the corona, where the electrons are thermally populated up to a certain energy, and then become non-thermal beyond the thermal cutoff.

The low electron temperature of the hard Comptonizing region could result from the energy balance within the hot flow or the efficient cooling by synchrotron photons produced by a hybrid electron plasma, which can

prevent the electrons from reaching higher temperatures.

We find from the reflection spectroscopy that the accretion disk is likely to be truncated away by at least $33 r_g$ from the ISCO in the HIMS, which also shows close agreement with the values estimated from modeling the disk continuum. The truncated disk scenario matches well with previous results reported for the bright LHS of other low-mass BHXRBs under the framework of dual Comptonizing regions ([Zdziarski et al. 2021b](#); [Banerjee et al. 2024](#); [Chand et al. 2024](#)).

The source exhibits a transition to the SIMS during Obs2 from the HIMS in Obs1 with an elevated disk temperature and a relatively steeper photon index. Unlike in the HIMS, the requirement of a single Comptonizing region to describe the broadband spectrum in the SIMS suggests a significant change in the coronal geometry across the state transition. This interpretation is further supported by the disk reaching relatively closer to the ISCO and a significant increase in the QPO frequency during the SIMS. However, the lack of high-energy data prevents us from probing the existence of a hard X-ray tail that may originate from the acceleration of a non-thermal electron population.

Our estimates of the black hole mass, spin, and disk inclination angle, obtained by modeling the disk continuum and reflection component together, broadly agree with the previously reported values. Within the uncertainties, these parameters are found to be consistent across the different models. Additionally, the distance to the source measured using model M5 closely matches the value reported by [Mata Sánchez et al. \(2025\)](#) based on optical spectroscopy.

The shape of the rms-energy spectra is consistent with those observed in the intermediate states of other low-mass BHXRBs. Our results indicate that the accretion disk remains relatively stable or only moderately variable, while the Comptonizing component exhibits strong variability in both spectral states. This behavior suggests that the overall source variability is primarily governed by the Comptonizing region.

6. ACKNOWLEDGMENTS

We would like to thank the anonymous reviewer for his/her comments that have helped to improve the quality of this paper. This research has made use of archival data from the NICER and NuSTAR missions, obtained from the High Energy Astrophysics Science Archive Research Center (HEASARC), provided by NASA’s Goddard Space Flight Center. It also makes use of data from the CZTI instrument onboard AstroSat, a mission of the Indian Space Research Organisation (ISRO),

with data archived at the Indian Space Science Data Centre (ISSDC). This work utilized data and software from the Insight-HXMT mission, a project funded by the China National Space Administration (CNSA) and the Chinese Academy of Sciences (CAS). We also acknowledge the use of data from the MAXI mission provided by RIKEN, JAXA, and the MAXI team. SC acknowledges support from the Polish Academy of Sciences through their study visit program. AAZ acknowledges support from the Polish National Science Center grants 2019/35/B/ST9/03944 and 2023/48/Q/ST9/00138.

Facilities: NICER, NuSTAR, AstroSat, Insight-HXMT, and MAXI.

Software: HEASoft (v.6.34; [Nasa High Energy Astrophysics Science Archive Research Center \(Heasarc\) 2014](#)), XSPEC (v.12.14.1; [Arnaud 1996](#)), CZTPIPELINE (v.3.0.1; <http://astrosat-ssc.iucaa.in/cztiData>), HXMTDAS (v.2.06; [Zhao 2020](#)), Stingray ([Huppenkothen et al. 2019a,b](#)), Matplotlib ([Hunter 2007](#)).

REFERENCES

- Agrawal, P. C., Yadav, J. S., Antia, H. M., et al. 2017, *Journal of Astrophysics and Astronomy*, 38, 30, doi: [10.1007/s12036-017-9451-z](https://doi.org/10.1007/s12036-017-9451-z)
- Antia, H. M., Yadav, J. S., Agrawal, P. C., et al. 2017, *ApJS*, 231, 10, doi: [10.3847/1538-4365/aa7a0e](https://doi.org/10.3847/1538-4365/aa7a0e)
- Arnaud, K. A. 1996, in *Astronomical Society of the Pacific Conference Series*, Vol. 101, *Astronomical Data Analysis Software and Systems V*, ed. G. H. Jacoby & J. Barnes, 17
- Bachetti, M., & Huppenkothen, D. 2018, *ApJL*, 853, L21, doi: [10.3847/2041-8213/aaa83b](https://doi.org/10.3847/2041-8213/aaa83b)
- Bachetti, M., Harrison, F. A., Cook, R., et al. 2015, *ApJ*, 800, 109, doi: [10.1088/0004-637X/800/2/109](https://doi.org/10.1088/0004-637X/800/2/109)
- Bambi, C., Brenneman, L. W., Dauser, T., et al. 2021, *SSRv*, 217, 65, doi: [10.1007/s11214-021-00841-8](https://doi.org/10.1007/s11214-021-00841-8)
- Banerjee, S., Dewangan, G. C., Knigge, C., et al. 2024, *ApJ*, 964, 189, doi: [10.3847/1538-4357/ad24ef](https://doi.org/10.3847/1538-4357/ad24ef)
- Belloni, T., Homan, J., Casella, P., et al. 2005, *A&A*, 440, 207, doi: [10.1051/0004-6361:20042457](https://doi.org/10.1051/0004-6361:20042457)
- Belloni, T. M. 2010, in *Lecture Notes in Physics*, Berlin Springer Verlag, ed. T. Belloni, Vol. 794, 53, doi: [10.1007/978-3-540-76937-8_3](https://doi.org/10.1007/978-3-540-76937-8_3)
- Belloni, T. M., Motta, S. E., & Muñoz-Darias, T. 2011, *Bulletin of the Astronomical Society of India*, 39, 409, doi: [10.48550/arXiv.1109.3388](https://doi.org/10.48550/arXiv.1109.3388)
- Cadotte, M., Sizun, P., Goldwurm, A., et al. 2006, *A&A*, 446, 591, doi: [10.1051/0004-6361:20053068](https://doi.org/10.1051/0004-6361:20053068)
- Cangemi, F., Rodriguez, J., Belloni, T., et al. 2023, *A&A*, 669, A65, doi: [10.1051/0004-6361/202243564](https://doi.org/10.1051/0004-6361/202243564)
- Cangemi, F., Beuchert, T., Siegert, T., et al. 2021, *A&A*, 650, A93, doi: [10.1051/0004-6361/202038604](https://doi.org/10.1051/0004-6361/202038604)
- Cao, X., Jiang, W., Meng, B., et al. 2020, *Science China Physics, Mechanics, and Astronomy*, 63, 249504, doi: [10.1007/s11433-019-1506-1](https://doi.org/10.1007/s11433-019-1506-1)
- Capitanio, F., Belloni, T., Del Santo, M., & Ubertini, P. 2009, *MNRAS*, 398, 1194, doi: [10.1111/j.1365-2966.2009.15196.x](https://doi.org/10.1111/j.1365-2966.2009.15196.x)
- Casella, P., Belloni, T., Homan, J., & Stella, L. 2004, *A&A*, 426, 587, doi: [10.1051/0004-6361:20041231](https://doi.org/10.1051/0004-6361:20041231)
- Casella, P., Belloni, T., & Stella, L. 2005, *ApJ*, 629, 403, doi: [10.1086/431174](https://doi.org/10.1086/431174)
- Chand, S., Dewangan, G. C., Thakur, P., Tripathi, P., & Agrawal, V. K. 2022, *ApJ*, 933, 69, doi: [10.3847/1538-4357/ac7154](https://doi.org/10.3847/1538-4357/ac7154)
- Chand, S., Dewangan, G. C., Zdziarski, A. A., et al. 2024, *ApJ*, 972, 20, doi: [10.3847/1538-4357/ad5a88](https://doi.org/10.3847/1538-4357/ad5a88)
- Chatterjee, K., Mondal, S., Singh, C. B., & Sugizaki, M. 2024, *ApJ*, 977, 148, doi: [10.3847/1538-4357/ad8dc4](https://doi.org/10.3847/1538-4357/ad8dc4)
- Chattopadhyay, T., Kumar, A., Rao, A. R., et al. 2024, *ApJL*, 960, L2, doi: [10.3847/2041-8213/ad118d](https://doi.org/10.3847/2041-8213/ad118d)
- Chen, Y., Cui, W., Li, W., et al. 2020, *Science China Physics, Mechanics, and Astronomy*, 63, 249505, doi: [10.1007/s11433-019-1469-5](https://doi.org/10.1007/s11433-019-1469-5)
- Dauser, T., Garcia, J., Parker, M. L., Fabian, A. C., & Wilms, J. 2014, *MNRAS*, 444, L100, doi: [10.1093/mnras/llu125](https://doi.org/10.1093/mnras/llu125)
- Davis, S. W., Blaes, O. M., Hubeny, I., & Turner, N. J. 2005, *ApJ*, 621, 372, doi: [10.1086/427278](https://doi.org/10.1086/427278)
- Davis, S. W., & Hubeny, I. 2006, *ApJS*, 164, 530, doi: [10.1086/503549](https://doi.org/10.1086/503549)
- Debnath, D., Chang, H.-K., Nath, S. K., & Titarchuk, L. 2025, *arXiv e-prints*, arXiv:2504.16391, doi: [10.48550/arXiv.2504.16391](https://doi.org/10.48550/arXiv.2504.16391)
- Debnath, D., Nath, S. K., Chatterjee, D., Chatterjee, K., & Chang, H.-K. 2024, *ApJ*, 975, 194, doi: [10.3847/1538-4357/ad7a76](https://doi.org/10.3847/1538-4357/ad7a76)
- Done, C., & Diaz Trigo, M. 2010, *MNRAS*, 407, 2287, doi: [10.1111/j.1365-2966.2010.17092.x](https://doi.org/10.1111/j.1365-2966.2010.17092.x)
- Done, C., & Gierliński, M. 2006, *MNRAS*, 367, 659, doi: [10.1111/j.1365-2966.2005.09968.x](https://doi.org/10.1111/j.1365-2966.2005.09968.x)
- Done, C., Gierliński, M., & Kubota, A. 2007, *A&A Rv*, 15, 1, doi: [10.1007/s00159-007-0006-1](https://doi.org/10.1007/s00159-007-0006-1)
- Fabian, A. C., Rees, M. J., Stella, L., & White, N. E. 1989, *MNRAS*, 238, 729, doi: [10.1093/mnras/238.3.729](https://doi.org/10.1093/mnras/238.3.729)

- Fender, R. P., Homan, J., & Belloni, T. M. 2009, *MNRAS*, 396, 1370, doi: [10.1111/j.1365-2966.2009.14841.x](https://doi.org/10.1111/j.1365-2966.2009.14841.x)
- García, J., Dauser, T., Lohfink, A., et al. 2014, *ApJ*, 782, 76, doi: [10.1088/0004-637X/782/2/76](https://doi.org/10.1088/0004-637X/782/2/76)
- García, J. A., Kallman, T. R., Bautista, M., et al. 2018, in *Astronomical Society of the Pacific Conference Series*, Vol. 515, Workshop on Astrophysical Opacities, 282, doi: [10.48550/arXiv.1805.00581](https://doi.org/10.48550/arXiv.1805.00581)
- García, J. A., Steiner, J. F., McClintock, J. E., et al. 2015, *ApJ*, 813, 84, doi: [10.1088/0004-637X/813/2/84](https://doi.org/10.1088/0004-637X/813/2/84)
- García, J. A., Tomsick, J. A., Sridhar, N., et al. 2019, *ApJ*, 885, 48, doi: [10.3847/1538-4357/ab384f](https://doi.org/10.3847/1538-4357/ab384f)
- Gendreau, K. C., Arzoumanian, Z., Adkins, P. W., et al. 2016, in *Society of Photo-Optical Instrumentation Engineers (SPIE) Conference Series*, Vol. 9905, Space Telescopes and Instrumentation 2016: Ultraviolet to Gamma Ray, ed. J.-W. A. den Herder, T. Takahashi, & M. Bautz, 99051H, doi: [10.1117/12.2231304](https://doi.org/10.1117/12.2231304)
- Gierliński, M., & Zdziarski, A. A. 2005, *MNRAS*, 363, 1349, doi: [10.1111/j.1365-2966.2005.09527.x](https://doi.org/10.1111/j.1365-2966.2005.09527.x)
- Gierliński, M., Zdziarski, A. A., Poutanen, J., et al. 1999, *MNRAS*, 309, 496, doi: [10.1046/j.1365-8711.1999.02875.x](https://doi.org/10.1046/j.1365-8711.1999.02875.x)
- Harrison, F. A., Craig, W. W., Christensen, F. E., et al. 2013, *ApJ*, 770, 103, doi: [10.1088/0004-637X/770/2/103](https://doi.org/10.1088/0004-637X/770/2/103)
- Homan, J., & Belloni, T. 2005, *Ap&SS*, 300, 107, doi: [10.1007/s10509-005-1197-4](https://doi.org/10.1007/s10509-005-1197-4)
- Homan, J., Wijnands, R., van der Klis, M., et al. 2001, *ApJS*, 132, 377, doi: [10.1086/318954](https://doi.org/10.1086/318954)
- Hunter, J. D. 2007, *Computing in Science and Engineering*, 9, 90, doi: [10.1109/MCSE.2007.55](https://doi.org/10.1109/MCSE.2007.55)
- Huppenkothen, D., Bachetti, M., Stevens, A., et al. 2019a, *The Journal of Open Source Software*, 4, 1393, doi: [10.21105/joss.01393](https://doi.org/10.21105/joss.01393)
- Huppenkothen, D., Bachetti, M., Stevens, A. L., et al. 2019b, *ApJ*, 881, 39, doi: [10.3847/1538-4357/ab258d](https://doi.org/10.3847/1538-4357/ab258d)
- Ingram, A., Bollemeijer, N., Veledina, A., et al. 2024, *ApJ*, 968, 76, doi: [10.3847/1538-4357/ad3faf](https://doi.org/10.3847/1538-4357/ad3faf)
- Jiang, J., Fabian, A. C., Wang, J., et al. 2019, *MNRAS*, 484, 1972, doi: [10.1093/mnras/stz095](https://doi.org/10.1093/mnras/stz095)
- Jourdain, E., Roques, J. P., & Malzac, J. 2012, *ApJ*, 744, 64, doi: [10.1088/0004-637X/744/1/64](https://doi.org/10.1088/0004-637X/744/1/64)
- Kaastra, J. S., & Bleeker, J. A. M. 2016, *A&A*, 587, A151, doi: [10.1051/0004-6361/201527395](https://doi.org/10.1051/0004-6361/201527395)
- Kennea, J. A., & Swift Team. 2023, *GRB Coordinates Network*, 34540, 1
- Kolehmainen, M., Done, C., & Díaz Trigo, M. 2014, *MNRAS*, 437, 316, doi: [10.1093/mnras/stt1886](https://doi.org/10.1093/mnras/stt1886)
- Li, L.-X., Zimmerman, E. R., Narayan, R., & McClintock, J. E. 2005, *ApJS*, 157, 335, doi: [10.1086/428089](https://doi.org/10.1086/428089)
- Liu, C., Zhang, Y., Li, X., et al. 2020, *Science China Physics, Mechanics, and Astronomy*, 63, 249503, doi: [10.1007/s11433-019-1486-x](https://doi.org/10.1007/s11433-019-1486-x)
- Liu, H.-X., Xu, Y.-J., Zhang, S.-N., et al. 2024, *arXiv e-prints*, arXiv:2406.03834, doi: [10.48550/arXiv.2406.03834](https://doi.org/10.48550/arXiv.2406.03834)
- Mahmoud, R. D., & Done, C. 2018, *MNRAS*, 480, 4040, doi: [10.1093/mnras/sty2133](https://doi.org/10.1093/mnras/sty2133)
- Mahmoud, R. D., Done, C., & De Marco, B. 2019, *MNRAS*, 486, 2137, doi: [10.1093/mnras/stz933](https://doi.org/10.1093/mnras/stz933)
- Malzac, J., & Belmont, R. 2009, *MNRAS*, 392, 570, doi: [10.1111/j.1365-2966.2008.14142.x](https://doi.org/10.1111/j.1365-2966.2008.14142.x)
- Mata Sánchez, D., Torres, M. A. P., Casares, J., et al. 2025, *A&A*, 693, A129, doi: [10.1051/0004-6361/202451960](https://doi.org/10.1051/0004-6361/202451960)
- McConnell, M. L., Ryan, J. M., Collmar, W., et al. 2000, *ApJ*, 543, 928, doi: [10.1086/317128](https://doi.org/10.1086/317128)
- McConnell, M. L., Zdziarski, A. A., Bennett, K., et al. 2002, *ApJ*, 572, 984, doi: [10.1086/340436](https://doi.org/10.1086/340436)
- Miller, J. M., Homan, J., Steeghs, D., et al. 2006, *ApJ*, 653, 525, doi: [10.1086/508644](https://doi.org/10.1086/508644)
- Miller, J. M., Reynolds, C. S., Fabian, A. C., et al. 2008, *ApJL*, 679, L113, doi: [10.1086/589446](https://doi.org/10.1086/589446)
- Mitsuda, K., Inoue, H., Koyama, K., et al. 1984, *PASJ*, 36, 741
- Nandi, A., Das, S., Majumder, S., et al. 2024, *MNRAS*, 531, 1149, doi: [10.1093/mnras/stae1208](https://doi.org/10.1093/mnras/stae1208)
- Nasa High Energy Astrophysics Science Archive Research Center (Heasarc). 2014, *HEASoft: Unified Release of FTOOLS and XANADU*, Astrophysics Source Code Library, record ascl:1408.004. <http://ascl.net/1408.004>
- Negoro, H., Serino, M., Nakajima, M., et al. 2023, *GRB Coordinates Network*, 34544, 1
- Page, K. L., Dichiara, S., Gropp, J. D., et al. 2023, *GRB Coordinates Network*, 34537, 1
- Palmer, D. M., & Parsotan, T. M. 2023, *The Astronomer's Telegram*, 16215, 1
- Peng, J.-Q., Zhang, S., Shui, Q.-C., et al. 2024, *ApJL*, 960, L17, doi: [10.3847/2041-8213/ad17ca](https://doi.org/10.3847/2041-8213/ad17ca)
- Poutanen, J., & Svensson, R. 1996, *ApJ*, 470, 249, doi: [10.1086/177865](https://doi.org/10.1086/177865)
- Poutanen, J., & Vurm, I. 2009, *ApJL*, 690, L97, doi: [10.1088/0004-637X/690/2/L97](https://doi.org/10.1088/0004-637X/690/2/L97)
- Rawat, D., Méndez, M., García, F., & Maggi, P. 2025, *A&A*, 697, A229, doi: [10.1051/0004-6361/202453538](https://doi.org/10.1051/0004-6361/202453538)
- Reis, R. C., Fabian, A. C., Ross, R. R., et al. 2008, *MNRAS*, 387, 1489, doi: [10.1111/j.1365-2966.2008.13358.x](https://doi.org/10.1111/j.1365-2966.2008.13358.x)
- Sahu, P., Chand, S., Dewangan, G. C., et al. 2025, *arXiv e-prints*, arXiv:2511.06393, doi: [10.48550/arXiv.2511.06393](https://doi.org/10.48550/arXiv.2511.06393)

- Sahu, P., Chand, S., Thakur, P., et al. 2024, *ApJ*, 975, 165, doi: [10.3847/1538-4357/ad7a6d](https://doi.org/10.3847/1538-4357/ad7a6d)
- Shakura, N. I., & Sunyaev, R. A. 1973, *A&A*, 24, 337
- Shimura, T., & Takahara, F. 1995, *ApJ*, 445, 780, doi: [10.1086/175740](https://doi.org/10.1086/175740)
- Singh, A., Sanna, A., Bhattacharyya, S., et al. 2025, *MNRAS*, 536, 1323, doi: [10.1093/mnras/stae2640](https://doi.org/10.1093/mnras/stae2640)
- Singh, K. P., Stewart, G. C., Chandra, S., et al. 2016, in *Society of Photo-Optical Instrumentation Engineers (SPIE) Conference Series*, Vol. 9905, *Space Telescopes and Instrumentation 2016: Ultraviolet to Gamma Ray*, ed. J.-W. A. den Herder, T. Takahashi, & M. Bautz, 99051E, doi: [10.1117/12.2235309](https://doi.org/10.1117/12.2235309)
- Singh, K. P., Stewart, G. C., Westergaard, N. J., et al. 2017, *Journal of Astrophysics and Astronomy*, 38, 29, doi: [10.1007/s12036-017-9448-7](https://doi.org/10.1007/s12036-017-9448-7)
- Steiner, J. F., Nathan, E., Hu, K., et al. 2024, *ApJL*, 969, L30, doi: [10.3847/2041-8213/ad58e4](https://doi.org/10.3847/2041-8213/ad58e4)
- Stiele, H., & Yu, W. 2016, *MNRAS*, 460, 1946, doi: [10.1093/mnras/stw821](https://doi.org/10.1093/mnras/stw821)
- Svoboda, J., Dovčiak, M., Steiner, J. F., et al. 2024, *ApJL*, 966, L35, doi: [10.3847/2041-8213/ad402e](https://doi.org/10.3847/2041-8213/ad402e)
- Tandon, S. N., Subramaniam, A., Girish, V., et al. 2017, *AJ*, 154, 128, doi: [10.3847/1538-3881/aa8451](https://doi.org/10.3847/1538-3881/aa8451)
- Tandon, S. N., Postma, J., Joseph, P., et al. 2020, *AJ*, 159, 158, doi: [10.3847/1538-3881/ab72a3](https://doi.org/10.3847/1538-3881/ab72a3)
- Vadawale, S. V., Rao, A. R., Bhattacharya, D., et al. 2016, in *Society of Photo-Optical Instrumentation Engineers (SPIE) Conference Series*, Vol. 9905, *Space Telescopes and Instrumentation 2016: Ultraviolet to Gamma Ray*, ed. J.-W. A. den Herder, T. Takahashi, & M. Bautz, 99051G, doi: [10.1117/12.2235373](https://doi.org/10.1117/12.2235373)
- Veledina, A., Poutanen, J., & Vurm, I. 2011, *ApJL*, 737, L17, doi: [10.1088/2041-8205/737/1/L17](https://doi.org/10.1088/2041-8205/737/1/L17)
- Veledina, A., Muleri, F., Dovčiak, M., et al. 2023, *ApJL*, 958, L16, doi: [10.3847/2041-8213/ad0781](https://doi.org/10.3847/2041-8213/ad0781)
- Verner, D. A., Ferland, G. J., Korista, K. T., & Yakovlev, D. G. 1996, *ApJ*, 465, 487, doi: [10.1086/177435](https://doi.org/10.1086/177435)
- Vibhute, A., Bhattacharya, D., Mithun, N. P. S., et al. 2021, *Journal of Astrophysics and Astronomy*, 42, 76, doi: [10.1007/s12036-021-09762-y](https://doi.org/10.1007/s12036-021-09762-y)
- Wardziński, G., Zdziarski, A. A., Gierliński, M., et al. 2002, *MNRAS*, 337, 829, doi: [10.1046/j.1365-8711.2002.05914.x](https://doi.org/10.1046/j.1365-8711.2002.05914.x)
- Wilms, J., Allen, A., & McCray, R. 2000, *ApJ*, 542, 914, doi: [10.1086/317016](https://doi.org/10.1086/317016)
- Yadav, J. S., Agrawal, P. C., Antia, H. M., et al. 2016a, in *Society of Photo-Optical Instrumentation Engineers (SPIE) Conference Series*, Vol. 9905, *Space Telescopes and Instrumentation 2016: Ultraviolet to Gamma Ray*, ed. J.-W. A. den Herder, T. Takahashi, & M. Bautz, 99051D, doi: [10.1117/12.2231857](https://doi.org/10.1117/12.2231857)
- Yadav, J. S., Misra, R., Verdhhan Chauhan, J., et al. 2016b, *ApJ*, 833, 27, doi: [10.3847/0004-637X/833/1/27](https://doi.org/10.3847/0004-637X/833/1/27)
- Zdziarski, A. A., Banerjee, S., Chand, S., et al. 2024a, *ApJ*, 962, 101, doi: [10.3847/1538-4357/ad1b60](https://doi.org/10.3847/1538-4357/ad1b60)
- Zdziarski, A. A., Dzielak, M. A., De Marco, B., Szanecki, M., & Niedźwiecki, A. 2021a, *ApJL*, 909, L9, doi: [10.3847/2041-8213/abe7ef](https://doi.org/10.3847/2041-8213/abe7ef)
- . 2021b, *ApJL*, 909, L9, doi: [10.3847/2041-8213/abe7ef](https://doi.org/10.3847/2041-8213/abe7ef)
- Zdziarski, A. A., & Gierliński, M. 2004, *Progress of Theoretical Physics Supplement*, 155, 99, doi: [10.1143/PTPS.155.99](https://doi.org/10.1143/PTPS.155.99)
- Zdziarski, A. A., Grove, J. E., Poutanen, J., Rao, A. R., & Vadawale, S. V. 2001, *ApJL*, 554, L45, doi: [10.1086/320932](https://doi.org/10.1086/320932)
- Zdziarski, A. A., Marcel, G., Veledina, A., Olejak, A., & Lancova, D. 2025a, *arXiv e-prints*, arXiv:2506.00623, doi: [10.48550/arXiv.2506.00623](https://doi.org/10.48550/arXiv.2506.00623)
- Zdziarski, A. A., Szanecki, M., Poutanen, J., Gierliński, M., & Biernacki, P. 2020, *MNRAS*, 492, 5234, doi: [10.1093/mnras/staa159](https://doi.org/10.1093/mnras/staa159)
- Zdziarski, A. A., Wood, C. M., & Carotenuto, F. 2025b, *ApJL*, 986, L35, doi: [10.3847/2041-8213/ade13b](https://doi.org/10.3847/2041-8213/ade13b)
- Zdziarski, A. A., You, B., Szanecki, M., Li, X.-B., & Ge, M. 2022, *ApJ*, 928, 11, doi: [10.3847/1538-4357/ac54a7](https://doi.org/10.3847/1538-4357/ac54a7)
- Zdziarski, A. A., Jourdain, E., Lubiński, P., et al. 2021c, *ApJL*, 914, L5, doi: [10.3847/2041-8213/ac0147](https://doi.org/10.3847/2041-8213/ac0147)
- Zdziarski, A. A., Chand, S., Banerjee, S., et al. 2024b, *ApJL*, 967, L9, doi: [10.3847/2041-8213/ad43ed](https://doi.org/10.3847/2041-8213/ad43ed)
- Zhang, S., Lu, F. J., Zhang, S. N., & Li, T. P. 2014, in *Society of Photo-Optical Instrumentation Engineers (SPIE) Conference Series*, Vol. 9144, *Space Telescopes and Instrumentation 2014: Ultraviolet to Gamma Ray*, ed. T. Takahashi, J.-W. A. den Herder, & M. Bautz, 914421, doi: [10.1117/12.2054144](https://doi.org/10.1117/12.2054144)
- Zhang, S., Zhang, S. N., Lu, F. J., et al. 2018, in *Society of Photo-Optical Instrumentation Engineers (SPIE) Conference Series*, Vol. 10699, *Space Telescopes and Instrumentation 2018: Ultraviolet to Gamma Ray*, ed. J.-W. A. den Herder, S. Nikzad, & K. Nakazawa, 106991U, doi: [10.1117/12.2311835](https://doi.org/10.1117/12.2311835)
- Zhang, S.-N., Li, T., Lu, F., et al. 2020, *Science China Physics, Mechanics, and Astronomy*, 63, 249502, doi: [10.1007/s11433-019-1432-6](https://doi.org/10.1007/s11433-019-1432-6)

Zhao, H. 2020, in Astronomical Society of the Pacific
Conference Series, Vol. 527, Astronomical Data Analysis
Software and Systems XXIX, ed. R. Pizzo, E. R. Deul,
J. D. Mol, J. de Plaa, & H. Verhouwer, 469